Dpp gradient formation by dynamin-dependent endocytosis: receptor trafficking and the diffusion model

Karsten Kruse[1,*], Periklis Pantazis[2,*], Tobias Bollenbach[1], Frank Jülicher[1,†] and Marcos González-Gaitán[2,†]

[1]MPI for the Physics of Complex Systems, Nöthnitzerstrasse 38, 01187 Dresden, Germany
[2]MPI of Molecular Cell Biology and Genetics, Pfotenhauerstrasse 108, 01307 Dresden, Germany
*These authors contributed equally to this work
[†]Authors for correspondence (e-mail: gonzalez@mpi-cbg.de; julicher@mpipks-dresden.mpg.de)

Accepted 28 June 2004

Development 131, 4843-4856
Published by The Company of Biologists 2004
doi:10.1242/dev.01335

Summary

Developing cells acquire positional information by reading the graded distribution of morphogens. In *Drosophila*, the Dpp morphogen forms a long-range concentration gradient by spreading from a restricted source in the developing wing. It has been assumed that Dpp spreads by extracellular diffusion. Under this assumption, the main role of endocytosis in gradient formation is to downregulate receptors at the cell surface. These surface receptors bind to the ligand and thereby interfere with its long-range movement. Recent experiments indicate that Dpp spreading is mediated by Dynamin-dependent endocytosis in the target tissue, suggesting that extracellular diffusion alone cannot account for Dpp dispersal. Here, we perform a theoretical study of a model for morphogen spreading based on extracellular diffusion, which takes into account receptor binding and trafficking. We compare profiles of ligand and surface receptors obtained in this model with experimental data. To this end, we monitored directly the pool of surface receptors and extracellular Dpp with specific antibodies. We conclude that current models considering pure extracellular diffusion cannot explain the observed role of endocytosis during Dpp long-range movement.

Key words: *Drosophila*, Morphogens, TGFβ

Introduction

Morphogens are signaling molecules which are produced and secreted from a restricted region of a developing tissue and spread to form a graded profile of concentration. This concentration profile, also called gradient by developmental biologists, endows receiving cells with positional information. Indeed, cells in the target field interpret the gradient by responding with expression of different target genes above distinct concentration thresholds and thereby at different distances from the source. Secreted ligands of the TGF-beta, Wnt and Hh families among others have been shown to act as morphogens (reviewed by Tabata, 2001).

Although the concept of morphogenetic signaling, first formulated by Turing (Turing, 1952) and modified by Wolpert (Wolpert, 1969), has pervaded the field of developmental biology, the cell biological basis of the spreading phenomenon itself for each particular morphogen molecule is still a matter of controversy (reviewed by González-Gaitán, 2003; Vincent and Dubois, 2002). Two scenarios for the dominant mechanisms of transport have been mainly discussed: extracellular diffusion and planar transcytosis, i.e. endocytosis and resecretion of the ligand that is thereby transported through the cells (reviewed by González-Gaitán, 2003; Vincent and Dubois, 2002).

In the case of the *Drosophila* TGF-beta-superfamily homolog Dpp, both diffusion and planar transcytosis have been proposed as transport mechanisms (Entchev et al., 2000; Lander et al., 2002) (reviewed by González-Gaitán, 2003). Dpp is expressed within a narrow stripe of cells in the center of the developing wing epithelium (Basler and Struhl, 1994), from where it is secreted and forms a long-range gradient of concentration across 40 cell diameters (Entchev et al., 2000; Teleman and Cohen, 2000). In experiments in which Dpp is pulsed from the source, the graded profile of Dpp concentration expands rapidly and reaches its steady state range of 40 cell diameters in less than 8 hours (Entchev et al., 2000; Teleman and Cohen, 2000). In addition, Dpp spreads equally in all directions.

The proposal that intracellular Dpp trafficking is implicated in its long-range dispersal stemmed from mosaic experiments in which endocytosis was impaired in mutant patches of cells: the ‘shibire rescue assay’, the ‘shibire shadow assay’ and the ‘Rab mutant assays’ (Entchev et al., 2000). In the ‘shibire rescue assay’, the source is wild-type (WT), whereas the target tissue is endocytosis-defective because of a Dynamin thermosensitive mutation (*shibire^{ts1}*, *shi^{ts1}*) (Chen et al., 1991). In this condition, Dpp is not internalized in the target cells and its range is restricted to the cells adjacent to the source. In the ‘shibire shadow assay’, Dpp spreading from the source is confronted with an endocytosis-defective mutant patch of cell. In this situation, Dpp is unable to spread across the clone and forms a shadow distal to the clone. The shadow is transient and is finally filled by Dpp moving rapidly and in all directions from the sides of the clone. Finally, in the ‘Rab mutant assay’,

mutants for key Rab GTPases involved in the endocytosis/early endosomal dynamics (Rab5) or degradation (Rab7) are expressed in the receiving cells. When endocytosis is impaired or degradation is enhanced, the signaling range is reduced, whereas, conversely, an enhanced endocytosis/endosomal dynamics leads to an expansion of the signaling range. These data support the idea that Dpp dispersal is mediated by endocytosis and resecretion of the ligand in the receiving cells. In the absence of endocytosis, extracellular diffusion contributes only to spreading over a short-range (across 3-5 cells) (Entchev et al., 2000). However, the Dpp re-secretion event itself has not yet been directly monitored.

In general, ligand transport depends on complex non-linear kinetics, such as the kinetics of receptor binding/release and the kinetics of trafficking of ligands and receptors. Therefore, a quantitative analysis based on mathematical models is essential in order to establish that the observed ligand dynamics indeed emerge from a particular mechanism. Ligand dispersal has been early described theoretically using reaction-diffusion equations (Gierer, 1981; Gierer and Meinhardt, 1972; Koch and Meinhardt, 1994; Turing, 1952). Such theoretical approaches are useful to study robustness and precision in morphogen gradient formation (Eldar et al., 2002; Eldar et al., 2003; Houchmandzadeh et al., 2002) and have suggested that simple diffusion may not suffice to generate graded profiles of receptor occupation (Kerszberg and Wolpert, 1998). Furthermore, ligand trafficking in cells has been studied theoretically and a possible role of transcytosis to enhance transport efficiency has been proposed (Chu et al., 1996; Lauffenburger and Linderman, 1993).

A recent theoretical analysis of Dpp spreading indicates, though, that transcytosis does not play an important part in this process (Lander et al., 2002). The properties of transport based on extracellular diffusion were studied using a model that takes into account diffusion and receptor binding. It was suggested that this ‘diffusion, binding and trafficking’ (DBT) model can generate ligand profiles which are consistent with WT gradients and the results observed in the ‘shibire shadow assay’ (Lander et al., 2002). A block of endocytosis could induce a higher level of surface receptors and thereby titrate out the pool of spreading free ligand, obstructing the ligand transport (Lecuit and Cohen, 1998). Lander et al. argued that this scenario generates a transient shadow. They solved reaction-diffusion equations in a one-dimensional geometry, suggesting that this description suffices to capture key features of these experiments.

Here, we perform a theoretical analysis of the DBT model in one and two dimensions. We discuss the role of the geometry, the appropriate boundary conditions, and the initial conditions in the ‘shibire shadow assay’ and the ‘shibire rescue assay’. We then determine experimentally the levels of receptors and extracellular Dpp to compare them with the ligand and receptor profiles obtained in the DBT model. We show that although the DBT model cannot account for the observed transient shadows, a modified version of the model, introducing surface receptor saturation, is consistent with such shadows. However, the receptor and ligand profiles under this modified DBT model are inconsistent with the observed levels in the ‘shibire shadow’ and ‘shibire rescue’ experiments. We therefore conclude that current models in which transport occurs exclusively in the form of extracellular diffusion cannot explain the experimental data, suggesting that endocytosis plays an active role in the ligand transport beyond the regulation of receptors at the surface.

Materials and methods

Numerical methods

Equations 1-7 together with boundary conditions have been solved numerically using a forward Euler differencing algorithm (see supplementary material). In the one-dimensional calculations, the area of interest (AOI) was discretized by 200 sites, and in our two-dimensional calculations, we used a triangular lattice with 200×174 sites. The time-step chosen was Δt=0.025 seconds for the one-dimensional and Δt=0.033 seconds for the two-dimensional calculations.

Mutant strains

shi^{ts1} and *tkv^{8}* are described in Flybase (http://flybase.bio.indiana.edu). *tkv^{8}* is a Tkv receptor truncated at amino acid 144 before the transmembrane domain that presumably represents a null mutation of *tkv* (Nellen et al., 1994). *UAS-Dynamin*, *UAS-Tkv* and *UAS-GFP-Dpp* were previously described (Entchev et al., 2000; Nellen et al., 1996). *UAS-GFP* was graciously provided by Barry Dickson (Institute of Molecular Pathology, Vienna, Austria). The *tub-DsRed* construct was inserted into a P-element plasmid containing the promoter of the tubulinα1 gene and flanked at its 3′ end by the 3′ UTR of the tubulinα1 gene (Basler and Struhl, 1994). *Tub-DsRed* was recombined onto FRT18 chromosome to allow the generation of somatic clones by Flp-mediated mitotic recombination (Xu and Harrison, 1994).

Antibodies and immunostainings

Rabbit anti-Tkv antibody was generated against two peptides corresponding to parts of the intracellular kinase domain (H2N-SQQLDPKQFEEFKRAC-CONH2 and H2N-GFRPPIPSR-WQEDDVC-CONH2). Rabbit luminal anti-Tkv antibody was generated against two peptides corresponding to the luminal side of the Tkv peptide sequence outside the ligand binding cleft (H2N-YEEERTYGCMPPEDNG-CONH2 and H2N-KEDFCNRDLYPT-YTP-CONH2). The immune sera were affinity chromatography purified using the corresponding Tkv peptides coupled to CNBr-activated Sepharose 4B (Amersham Biosciences). The specificity of the antibodies was tested by preincubating the purified antibody with 100 μg/ml Tkv peptide (or 500 μg/ml when performing the ‘extracellular immunostaining protocol with luminal anti-Tkv antibody’) for 30 minutes at room temperature and performing subsequently an antibody staining on Tkv-overexpressing discs. No fluorescent signal was detected under these conditions, whereas preincubation with a control peptide did not affect the staining. Immunostainings were performed as previously described (Entchev et al., 2000) using Mouse anti-Myc, 1:25 dilution; Rabbit anti-Tkv (intracellular), 1:125; Goat anti-GFP, 1:100. Extracellular GFP-Dpp and cell surface-exposed Tkv were detected by incubating prior to fixation (Strigini and Cohen, 2000) with Goat anti-GFP antibody, 1:10 dilution, and Rabbit anti-Tkv (raised against the luminal domain of Tkv), 1:10 dilution, respectively. Dimmer GFP-Dpp signal was found upon extracellular immunostaining compared with the normal staining because of the different washing procedures. To estimate GFP-Dpp range in number of cells, a fluorescent phalloidin (Molecular Probes) counterstaining was performed to monitor the cell profiles. Cryostat z-sections at Cryo-Star HM 560 (Microm) were performed with PFA-fixed developing wing discs incubated for at least 12 hours at 4°C in 30% sucrose solution in PBS and mounted with Tissue-Tek (Sakura). Images were acquired in a Zeiss LSM510 confocal microscope and processed using Adobe Photoshop 7.0 (Adobe Systems). Quantifications were done with Image J (NIH).

Mosaics

tkv^{8} mutant Minute^{+}/FRT clones (Xu and Harrison, 1994) were generated by heat shock (30 minutes, 36°C) in 3-day-old larvae (*HS-Flp/+; M(2)z PMyc FRT40A/tkv*^{8} *FRT40A*) and raised at 25°C to mid-third-instar larvae. To induce PMyc transcription larvae were heat-shocked at 38°C for 1 hour followed by at least 1 hour at 25°C to allow the translation of the PMyc transcript prior to fixation. *shi*^{ts1} FRT mutant clones were generated in larvae of the genotype *shi*^{ts1} *FRT18A/HS-NM8A FRT18A; HS-Flp/+* and *shi*^{ts1} *FRT18A/tub-DsRed FRT18A; HS-Flp/+*, respectively. Embryos were collected during one day at 18°C, larvae were raised for one day at 18°C and heat-shocked (90 minutes, 38.3°C). Larvae were subsequently kept at 25°C until third-instar larval stage. Afterwards, endocytosis was blocked either for 3 hours at 34°C followed by 1 hour at 38.3°C to induce both NMyc transcription and shibire block and 1 hour at 34°C to allow the translation of the NMyc transcript, or for 5 hours at 34°C in the case of larvae of the genotype *shi*^{ts1} *FRT18A/tub-DsRed FRT18A; HS-Flp/+*. Dissection of wing discs was performed at 34°C.

Blockage of endocytosis at receiving cells

shi^{ts1}*; UAS-Dynamin*$^{+}$*/+; dpp-gal4/UAS-GFP-Dpp* larvae were kept at the *shi*^{ts1}-permissive temperature (25°C or 18°C) to allow normal wing development until third-instar larval stage, when endocytosis was blocked for 6 hours at 34°C. Wing discs were dissected and fixed.

Results

Mathematical description of Dpp transport by diffusion and receptor kinetics

We will consider the transport of Dpp throughout the primordium of the wing. As the wing disc is a single-layered epithelium (Fig. 1), the transport of Dpp occurs essentially in two dimensions. We therefore neglect the folding of the wing disc in three-dimensional space (Fig. 1B,D) and assume it to be planar. Positions on this plane will be specified by x and y coordinates (Fig. 1E). The transport of Dpp in the epithelium is characterized by the Dpp current $J=(J_x,J_y)$. This current is a vector with components J_x and J_y, quantifying the number of Dpp molecules that are transported per unit time across a line of unit length in x and y direction, respectively. In two dimensions, this current is measured in Moles s^{-1} m^{-1}. If transport is exclusively because of diffusion, the current is generated by gradients (i.e. local differences) in ligand concentration. Formally, this can be written as:

$$\begin{pmatrix} J_x \\ J_y \end{pmatrix} = -D_0 \begin{pmatrix} \frac{\partial A}{\partial x} \\ \frac{\partial A}{\partial y} \end{pmatrix}, \qquad (1)$$

where D_0 is the diffusion constant characterizing diffusion in the extracellular space and $A=[L]$ is the free extracellular ligand concentration. In the absence of any receptor binding and unbinding, the change per unit time of the ligand concentration A at a point (x,y) follows from the balance of currents in the plane. The rate of this change $\partial A/\partial t$ is given by:

$$\frac{\partial A}{\partial t} = -\frac{\partial J_x}{\partial x} - \frac{\partial J_y}{\partial y} = D_0\left(\frac{\partial^2}{\partial x^2} + \frac{\partial^2}{\partial y^2}\right)A\,. \qquad (2)$$

The concentration of free ligands varies not only because of diffusion: ligands bind to and detach from cell surface receptors. In addition, receptors traffic through both the biosynthetic and endocytic pathways. They appear at the plasma membrane, are internalized into cells by endocytosis and are degraded in the lysosomes (Fig. 2A). These processes affect both free and ligand-bound receptors. The full kinetics of the ligand and receptor concentrations is described by:

$$\frac{\partial A}{\partial t} = D_0 \Delta A - k_{on} A D + k_{off} B \qquad (3)$$

$$\frac{\partial B}{\partial t} = k_{on} A D - \left(k_{in} + k_{off}\right) B + k_{out} C \qquad (4)$$

$$\frac{\partial C}{\partial t} = k_{in} B - \left(k_{out} + k_{deg}\right) C \qquad (5)$$

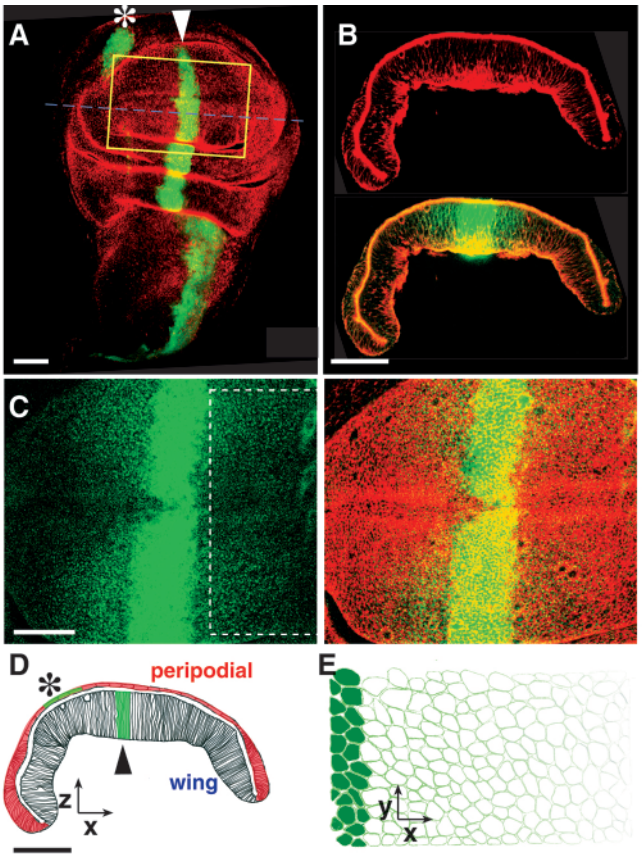

Fig. 1. Dpp signaling in the developing wing system. (A) Double staining of a developing wing showing the Dpp source (wing pouch, arrowhead; peripodial epithelium, asterisk) monitored by GFP (green) and cell profiles labelled with phalloidin (red). Genotype: *UAS-GFP/+; dpp-gal4/+*. (B) Double staining of a cryostat z-section of a developing wing at the level of the broken line in A, showing cell profiles labelled by phalloidin (red), superimposed by GFP-Dpp expression (green) in the lower panel. Genotype: *dpp-gal4/UAS-GFP-Dpp*. (C) Detail of GFP-Dpp localization (green) in the region of the developing wing corresponding to the yellow box in A. Phalloidin labeling (red) is superimposed to show cell profiles in the right panel. (D,E) Schematic representation of the developing wing in a xz- (D) and xy-section (E). Note the position of the Dpp source (cells filled in green to the left in E) both in the wing pouch (arrowhead) and the peripodial epithelium (red in D; asterisk). Scale bars: 50 μm. Anterior to the left.

$$\frac{\partial D}{\partial t} = k_{off}B + k_q E - k_{on}AD - k_p D \quad (6)$$

$$\frac{\partial E}{\partial t} = w + k_p D - \left(k_q + k_g\right)E\,, \quad (7)$$

where

$$\Delta = \frac{\partial^2}{\partial x^2} + \frac{\partial^2}{\partial y^2}$$

is a short notation for the Diffusion operator. Here, $B=[LR]_{out}$, is the concentration of ligand-bound receptors on cell surfaces, $C=[LR]_{in}$ is the concentration of ligand-bound receptors inside cells, $D=[R]_{out}$ and $E=[R]_{in}$ are the concentrations of free receptors outside and inside the cell, respectively (see also Fig. 2A). We have defined the on- and off-rates (i.e. binding and dissociation constants) for ligand-receptor binding k_{on} and k_{off} as well as the rates of endocytosis and exocytosis of ligand-bound receptors k_{in} and k_{out}. The degradation rate of internalized ligands bound to receptors is denoted by k_{deg}. Receptors are produced with biosynthetic rate w, internalized and recycled with rates k_p and k_q, and degraded with rate k_g. Equations 3-7 describe the dynamics of the Dpp distribution in the target tissue according to the DBT model. In summary, the DBT model assumes that transport is exclusively because of extracellular diffusion and takes into account binding to and release from the surface receptors. These receptors, in turn, traffic through the biosynthetic and endocytic pathways. Equations 3-7 correspond to model C described in Lander et al. (Lander et al., 2002) formulated here in two-dimensional geometry.

Geometry of the wing disc and area of interest

The wing disc forms a flat pouch consisting of two cell layers, which are connected at the edges (Fig. 1D). One cell layer is formed by columnar epithelial cells and includes the wing primordium (Fig. 1A,D; arrowhead); the other layer forms a squamous epithelium, the peripodial epithelium (Fig. 1A,D; asterisk). Dpp-producing cells are located within a narrow band, 5 cells wide, along the anterior-posterior compartment boundary (Fig. 1) in the center of both the columnar and the peripodial cell layer (Fig. 1D).

We are interested in the formation of a Dpp gradient in a particular area of the primordium. Fig. 1C and Fig. 2C define this AOI. The AOI corresponds to a rectangular piece of tissue in the primordial cell layer located in the posterior compartment and adjacent to the Dpp source (Fig. 1C, Fig. 2C). It extends L_x=200 μm (50 cells) in the x-direction and L_y=200 μm (50 cells) in the y-direction (Fig. 2C). In principle, we need to take into account the complete geometry of the wing disc in order to have a full mathematical description of the ligand kinetics. However, the ligand kinetics within the AOI depends only weakly on the kinetics outside, provided the size of the AOI is sufficiently large (see below).

Boundary conditions

Because we describe an AOI of finite extension, the currents of ligand entering and leaving the AOI at its boundaries have to be specified. Along the boundary adjacent to the secreting cells at x=0 (‘source boundary’; Fig. 2C), cells expressing Dpp inject the morphogen into the AOI. A cell of width a (approximately 4 μm) secretes Dpp at a constant rate, which is denoted by v and measured in Moles/s (Fig. 2A,C). A single cell contributes to a Dpp current into the AOI of magnitude $v/2a$ along the x-direction. Here, the factor two takes into account that Dpp leaves the source in two directions (towards anterior and posterior) and only half of the secreted ligand reaches the posterior compartment. The total current entering the AOI is increased by a factor d/a, which is the number of contributing cells. Here, d≈20 μm denotes the width of the stripe of secreting cells (Fig. 2C). For simplicity, we assume that the Dpp source is homogeneous along the y-direction. The source boundary condition at x=0 is thus given by:

$$J_x = vd/2a^2\,. \quad (8)$$

Note also that we have neglected degradation of ligand in the secreting cells. We have performed calculations where, instead of using condition (8), the secreting tissue has also been fully described by reaction-diffusion equations (see below the ‘shibire rescue assay’). These calculations show that, for a source with d=20 μm, condition (8) is a good approximation (not shown).

Let us consider the boundary at $x=L_x$ on the opposite side of the AOI with respect to the source (‘distal boundary’; Fig. 2C). An outflux of ligand across this boundary is present which becomes small if the ligand concentration nearby is small. We expect the current across the boundary sufficiently far from the source to be small enough to be neglected and impose the current to be zero at the boundary. We choose the width L_x of the AOI, such that this choice of boundary condition does not affect the ligand distribution in the region where the gradient develops. Indeed, one can show that for $L_x \geqslant 200$ μm the choice of the ‘distal boundary’ condition becomes irrelevant (see Fig. S3 in the supplementary material).

At the remaining boundary lines $y=-L_y/2$ and $y=+L_y/2$ of the AOI (‘side boundaries’; Fig. 2C), we also impose ‘zero current’ conditions across the boundary line, J_y=0. In the simplest case, in which the whole system is homogeneous in the y-direction, this condition is satisfied automatically. An example for the formation of a graded ligand profile using these boundary conditions (‘current boundary’ conditions) is displayed in Fig. 2D. A more interesting case arises if a patch of genetically modified cells (a clone) is present in the system. Then, ligand and receptor concentrations will vary along the y-coordinate and a current can cross the boundaries at $y=-L_y/2$ and $y=+L_y/2$. However, if the boundaries are located sufficiently far away from the clone, the ligand concentration in the vicinity of the clone is not affected by our choice of boundary conditions. For a clone of size 50 μm, we observed that the choice L_y=200 μm results in concentration profiles that are independent of the specific boundary conditions imposed (see supplementary material).

Dpp depletion behind *shi^{ts1}* clones

The role of endocytosis during Dpp gradient formation has been studied by inducing a patch of thermosensitive Dynamin mutant cells, a *shi^{ts1}* clone, into a wing disc (Entchev et al., 2000). In this experiment, GFP-Dpp expression in the source was triggered using the thermosensitivity of the driver system. The experiment is performed under the following initial conditions: (1) Non-tagged endogenous Dpp is also expressed in the disc and is presumably in a steady-state distribution,

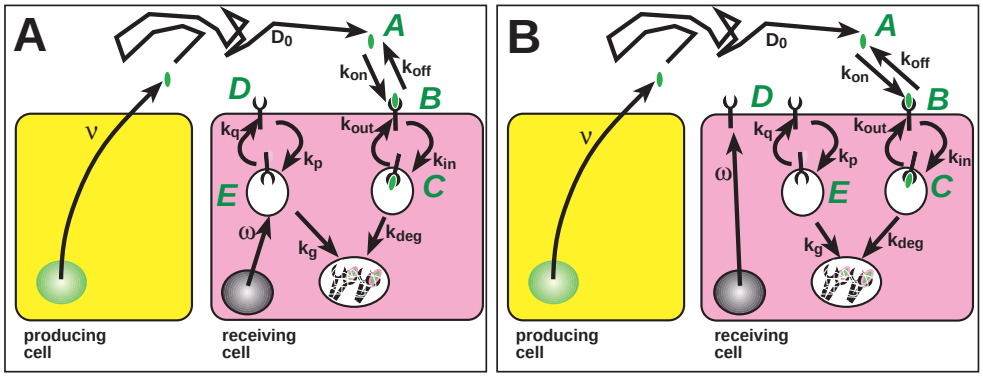

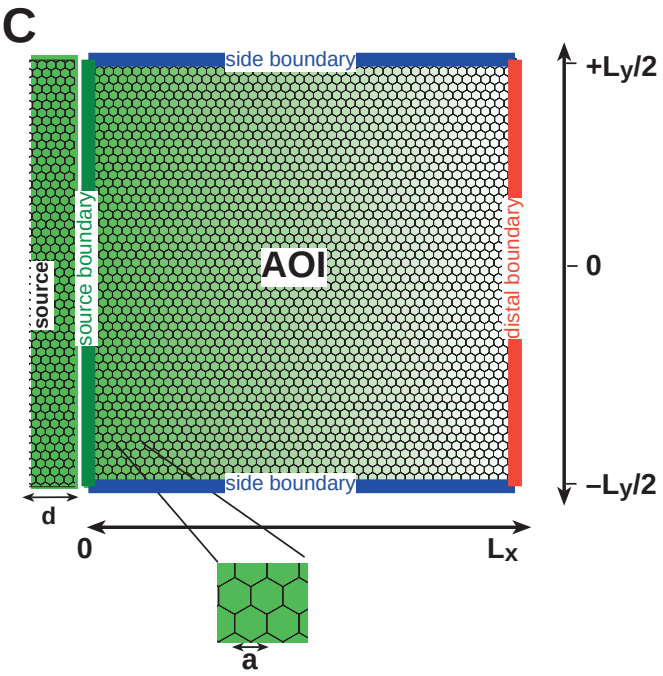

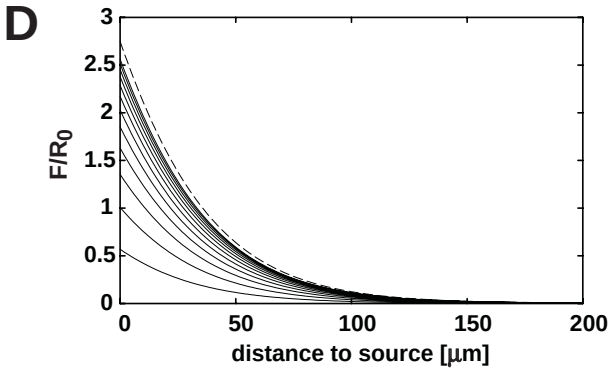

Fig. 2. Transport scheme, area of interest (AOI) and gradient formation in the DBT model. (A) Dpp transport scheme considered in this study and in Lander et al. (Lander et al., 2002). For further details, see main text. (B) Dpp transport scheme with biosynthetic route targeting the receptor directly to the plasma membrane (Alberts et al., 1994). (C) Simplified geometry of the AOI (corresponding to the broken box in Fig. 1C) as used in the calculations. (D) Total ligand concentration F (sum of free extracellular ligand concentration *A*, surface-bound ligand concentration *B*, and internal-bound ligand concentration *C*) as a function of the distance from the source calculated in the DBT model for different times. Unbroken curves are separated by intervals of 2 hours; broken curve corresponds to the steady state. The initial conditions were $A=B=C=0$, $D=R_0$, and $E=R_0k_p/k_q$ for all x. Note that the total ligand concentration has been displayed in ordinates normalized to $R_0=wk_q/k_gk_p$ which is a constant that corresponds to the steady-state surface receptor concentration in the absence of ligand.

because normal-looking adults emerge when applying these temperature conditions in WT animals; and (2) the thermosensitive Dynamin mutant cells can perform endocytosis at the permissive temperature (25°C) at $t=0$. The experiment starts by elevating the temperature (34°C), which causes an immediate block of endocytosis in the clone, and an immediate onset of GFP-Dpp production in the source.

Under these conditions, GFP-Dpp is entering the target tissue. When confronted with the endocytosis-defective Dynamin mutant clone, a 'shadow', a region with reduced GFP-Dpp concentration distal to the clone, is generated. This shadow can only be observed for a limited time: after several hours, the shadow region is indistinguishable from the adjacent regions. This result provides evidence that endocytosis is essential for the long-range movement of Dpp. Based on this and the 'shibire rescue assay' (see below), a working model was proposed in which free diffusion of Dpp only accounts for short-range spreading of Dpp, and long-range movement of Dpp is mediated by repeated rounds of internalization and re-secretion through the receiving cells (Entchev et al., 2000).

We now address the question of whether the DBT model can account for the formation of a transient shadow behind the clone. For this purpose, we solve the DBT dynamic Eqns 3-7 using the 'current boundary conditions' discussed above. We perform a two-dimensional calculation representing the clone by a rectangular region. In this region the internalization rates for the free- and the bound-receptor k_{in} and k_p are abruptly reduced at $t=0$ in order to model an impaired endocytosis.

A rapid reduction of the receptor internalization rates is consistent with the observation that endocytosis is blocked within seconds in the thermosensitive dynamin mutant (Entchev et al., 2000; Ramaswami et al., 1994). In the DBT model, completely blocking endocytosis would correspond to setting the internalization rates k_{in} and k_p to zero. However, this leads to an unrealistic unlimited increase of the cell surface receptor concentration. There are two obvious ways to limit the surface receptor concentration: introducing surface receptor saturation by defining the externalization rates of the receptor as a function of surface receptor concentration, and reducing internalization rates to a non-zero value. The effects of surface receptor saturation are discussed in the next section. In this section, the internalization rates are reduced by a factor of 10.

In our calculations, the initial receptor concentrations in the whole AOI are set to the WT steady-state values in the absence of ligands. The resulting concentration profiles in the presence of a clone are displayed in Fig. 3A-E. Behind the clone, the

concentration exhibits a clear minimum along the y-axis in the ligand concentration (Fig. 3A,E). This minimum reflects a depletion or 'shadow' that is reminiscent of the Dpp depletion observed by Entchev et al. However, in contrast to the experiments, in which the shadow disappeared with time, the DBT model does not generate transient shadows, but instead shadows become more pronounced with time and persist in the steady state (Fig. 3E). The contrast of the shadow can be quantified by comparing the total ligand concentrations at the points indicated by the arrows in Fig. 3E. As the Dpp gradient is built up, the contrast increases monotonously and attains a steady-state value with maximal contrast (Fig. 3F).

We have thus shown that, in the DBT model, shadows are generated that become more contrasted with time and remain persistent. Transient shadows as observed in the experiments are not obtained in the DBT model.

A DBT model with saturating cell surface receptor concentration (DBTS) can generate transient shadows behind a shibire clone

The DBT model becomes biologically meaningless if internalization rates become zero, because in this case the level of surface receptors tends to infinity. It is therefore not possible to describe the extreme case in which the endocytotic block is complete. However, at the restrictive temperature the internalization in shibire mutants is negligible (Entchev et al., 2000; Verstreken et al., 2002). Therefore, we modify the DBT model to include the saturation of surface receptor levels. This allows us to freely vary the internalization rates and even set them to zero.

Surface receptor levels saturate at some maximal density R_{max}. In the DBTS model (Diffusion, receptor binding and trafficking with surface receptor saturation), we assume that the rates of delivery to the plasma membrane ('externalization') of the free receptor k_q and that of the bound receptor k_{out} are a function of the total surface receptor level $B+D$ as follows:

$$k_q = k_q^0\left(1-\frac{B+D}{R_{max}}\right)$$
$$k_{out} = k_{out}^0\left(1-\frac{B+D}{R_{max}}\right). \quad (9)$$

Here, the parameters k_q^0 and k_{out}^0 are equal to the originally introduced externalization rates. For small surface receptor concentrations $B+D$, the DBTS model corresponds to the original DBT model. As $B+D$ approaches R_{max}, the externalization rates k_q and k_{out} tend to zero. In biological terms, this would correspond to a situation in which the externalization rates of the receptor depend on a limiting factor(s) that can thereby be saturated, such as the trafficking machinery, cargo receptors, etc.

The profiles of total (Fig. 4A-E) and internal bound (inset in Fig. 4C; see also Fig. 7E) Dpp have been obtained by a calculation of the DBTS model in two dimensions and in the presence of a clone. Inside the clone, the internalization rates

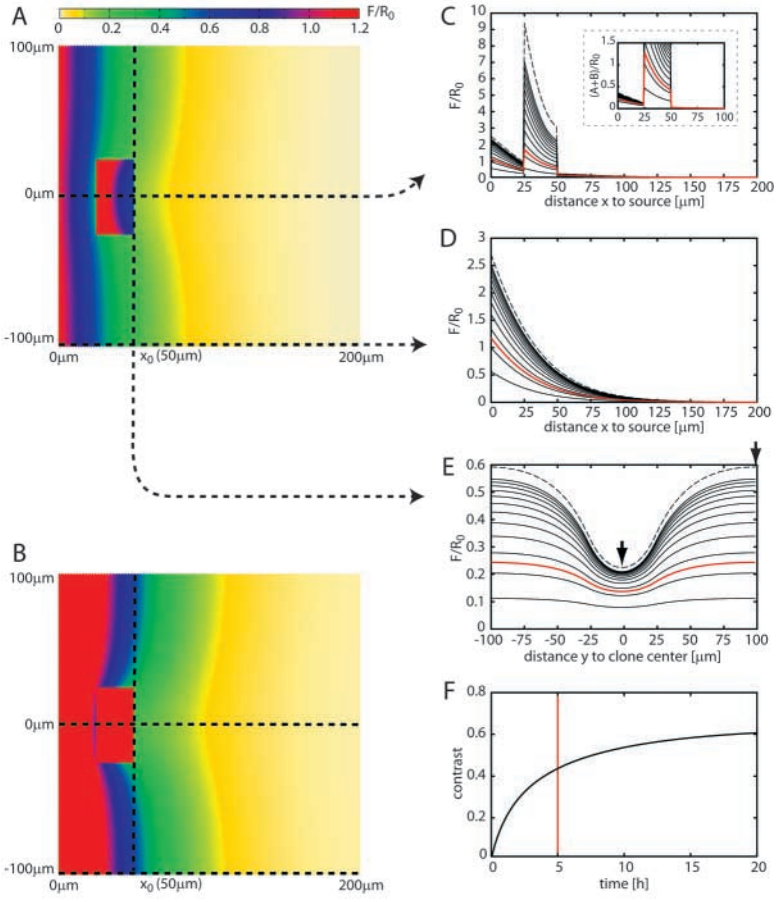

Fig. 3. Gradients in the DBT model describing a tissue with *shi*^{ts1} clone. Dynamics of the total ligand distribution F in the DBT model in an area of interest (AOI) of size L_x=200 µm and L_y=200 µm. The AOI contains a rectangular region, inside which the internalization rates k_p and k_{in} are reduced by a factor of 10 after t=0. This region covers the intervals 25 µm⩽x⩽50 µm and –25 µm⩽y⩽25 µm and describes the effects of a temperature shift on a shibire clone. (A) Color-coded distribution of the total ligand concentration $F=A+B+C$ at t=5 hours. (B) Distribution of F after 48 hours, which is close to the steady state. (C-E) Total ligand concentration F along the broken lines indicated in A,B. Unbroken black lines are separated by 2 hours. The red line represents the distributions after 5 hours, the time when the observations were made in the experiments discussed in Entchev et al. (Entchev et al., 2000); the broken lines represent the steady state distributions. Note the accumulation of ligand in the clone by a factor of 10. Far away from the clone, the ligand distribution resembles the distribution in absence of a clone (compare D with Fig. 2D). The steady-state ligand concentration has a pronounced minimum behind the center of the clone (E). The inset in C displays the profile of total extracellular ligand $A+B$. Note that the extracellular ligand accumulates in the clone by a factor of 10 after 5 hours of endocytotic block and more than 40 times in the steady state. (F) Contrast of the shadow as a function of time. The contrast c is defined as the difference in the total ligand concentration at the points indicated by arrows in E normalized with respect to the total ligand concentration at ($x=x_0$,$y=L_y/2$). Formally, $c=[F(x_0,L_y/2)-F(x_0,0)]/F(x_0,L_y/2)$. Note that the contrast still increases after 5 hours and that the shadow persists. Results in A-F were obtained by solving Eqns 3-7 with parameter values as given in Table 1 and 'current boundary conditions', given by $J_x=0$ at $x=L_x$, $J_x=vd/2a^2$ at $x=0$, $J_y=0$ at $y=\pm L_y/2$; initial conditions $A=B=C=0$, $D=R_0$, as well as $E=R_0k_p/k_q$.

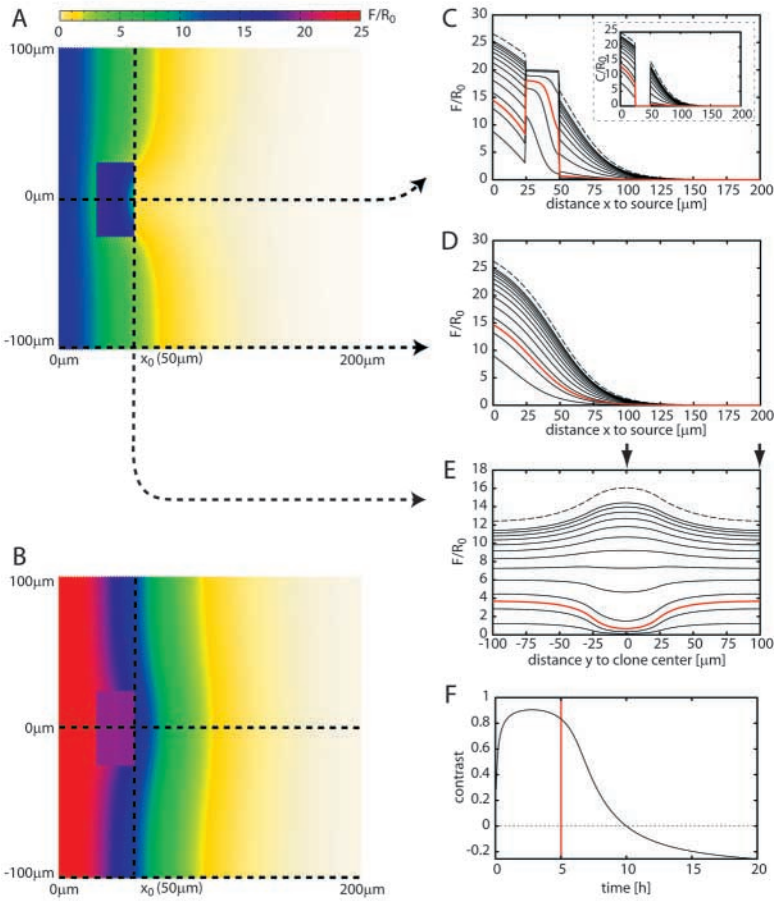

Fig. 4. Gradients in the DBTS model describing a tissue with *shi*^{ts1} clone. Evolution of the total ligand distribution as shown in Fig. 3, but in the DBTS model with vanishing internalization rates within a region describing the clone. (A,B) Color-coded distribution of the total ligand concentration $F=A+B+C$ after 5 hours of endocytic block (A), and after 48 hours, corresponding to the steady state (B). (C-E) Total ligand concentration F along the broken lines indicated in A,B. Unbroken black lines are separated by 2 hours. The broken lines represent the steady state distributions, the red line the distributions after 5 hours, the time when the observations were made in the experiments discussed in Entchev et al. (Entchev et al., 2000). The inset in C shows the concentration of internal-bound ligand, which vanishes inside the clone. The profile of the ligand concentration behind the clone is shown in E. At 5 hours, a clear shadow is present which vanishes and turns into a persistent anti-shadow. (F) Contrast c of the shadow as defined in Fig. 3. The results were obtained by solving Eqns 3-7 in a rectangular area of interest (AOI) of size L_x=200 µm and L_y=200 µm with parameter values indicated in Table 1, 'current boundary conditions', i.e., $J_x=0$ at $x=L_x$, $J_x=vd/2a^2$ at $x=0$, $J_y=0$ at $y=0$ as well as at $y=L_y$. At $t=0$ initial conditions were $A=B=C=0$, $D=R_0$, where $R_0=wk_q^0/k_gk_p$ and $E=k_p/k_q^0$. The internalization rates are given by Eqn 9 with $R_{max}=20R_0$.

k_p and k_{in} have been set to zero at $t=0$. The profile in the y-direction behind the clone displays a pronounced transient shadow similar to the experimental observation (Fig. 4A,C-E), followed by a weak persistent accumulation of ligand behind the clone ('anti-shadow') after long time periods (Fig. 4B-E). The corresponding contrast of this shadow attains a maximum after a few hours (Fig. 4F). The emergence of a shadow is a consequence of a rapid 20-fold increase of the surface receptor concentration inside the clone (Fig. 7G). In order to obtain such a rapid increase in the surface receptor concentration, the externalization and internalization rates had to be increased (by at least a factor of 10) compared with the values used in the DBT model (Table 1).

The models discussed so far assume that receptors produced de novo traffic through the secretory pathway via endocytic compartments (Fig. 2A). Although this biosynthetic trafficking pathway seems to exist in yeast cells (Harsay and Schekman, 2002), the conventional biosynthetic pathway does not necessarily involve endosomal structures (Alberts et al., 1994) (Fig. 2B). We therefore modified the DBTS model to consider the standard biosynthetic and endocytic pathways (Alberts et al., 1994) (see supplementary material). Numerical calculations show that this modification does not lead to major changes with respect to the DBTS model.

In summary, the DBTS model can generate Dpp profiles outside of the clone that qualitatively resemble the ones observed, although anti-shadows have not been observed experimentally. Note that the DBT and the DBTS model

Table 1. Parameter values used for the DBT and DBTS models in this paper

	DBT	DBTS	EGF
k_{off} (h^{-1})	0.036	0.036	20.40
k_{in} (h^{-1})	2.160	36.00	18.00
k_p (h^{-1})	2.160	21.60	1.800
k_{deg} (h^{-1})	0.119	0.119	0.120
k_g (h^{-1})	0.360	0.360	0.120
k_{out} (h^{-1})	0.241	2.412	3.480
k_q (h^{-1})	0.180	1.800	3.480
k_{on} R_0 (h^{-1})	43.20	144.0	–
ν/R_0 (h^{-1})	1.940	28.80	–
w/R_0 (h^{-1})	4.320	4.320	–
D′ (m^2/s)	10^{-11}	10^{-11}	–
R_0 (molecules/cell)	300	300	–
k_{on} (h^{-1})	0.144	0.480	0.224
ν (h^{-1})	583.0	8640	–
w (h^{-1})	1296	1296	7800

For details see text and Fig. 2. Parameter values measured for the EGF/EGF receptor system in B82 fibroblasts are given for comparison (Herbst et al., 1994; Lauffenburger and Linderman, 1993; Starbuck and Lauffenburger, 1992). The value of k_{on} has been converted to the units used in this paper by estimating a volume of the extracellular space per cell of 3.2×10^{-14} liters. The current of ligand into the AOI at $x=0$ is obtained from the ligand production rate ν via $J_x=vd/2a^2$, where d=20 µm and a=4 µm. The parameters used for the DBT model correspond to those used elsewhere (Lander et al., 2002) and are within the parameter space leading to the formation of shadows.

require a drastically increased surface receptor concentration within the clone in order to create significant shadows. This generates a large accumulation of surface-bound ligand inside the clone in both models.

The DBT and DBTS models are inconsistent with the observed ligand and receptor concentrations in shibire clones

The DBT model can generate morphogen gradients similar to those seen experimentally in the absence of a clone (Fig. 2D). In particular, the steady-state profiles of total Dpp and extracellular Dpp, monitored with a specific extracellular GFP-Dpp immunostaining (Strigini and Cohen, 1999) (Fig. 5), resemble the profiles obtained by the DBT model for total (Fig. 2D) and extracellular Dpp (not shown). In addition, the time needed to form the gradient upon a pulse of Dpp from the source (Fig. 2D) is consistent with experimental observations in which the gradient expands until it reaches a steady state 6 to 8 hours after the initiation of the pulse (Entchev et al., 2000).

In the presence of a *shi^{ts1}* clone, there are, however, important differences between the results of the DBT model and the experimental data. If we choose parameters in such a way that the ligand profiles define a shadow behind the clone, the levels of (1) surface receptors, (2) total ligands inside the endocytosis-defective shibire clone and (3) extracellular ligand observed experimentally are qualitatively different from those obtained in the DBT model. The same conclusion holds true for the DBTS model, in which the levels of total (Fig. 4C) and internalized ligand (Fig. 4C, inset) in the clone are also elevated, unlike our experimental observations.

We first consider the cell surface receptor concentration. The essential prerequisite for forming a shadow in the DBTS model is a rapid accumulation by a factor of 10-20 of surface receptors in the clone (Fig. 7G). In order to compare this with the actual surface receptor levels in the clone, we raised an antibody that specifically recognizes the Dpp receptor, Tkv. Confirming the results published in Teleman and Cohen (Teleman and Cohen, 2000), we find that the receptor accumulates predominantly at the cell surface, although some intracellular vesicular structures can also be observed (see Fig. S5A in the supplementary material). The level of the Tkv protein follows the accumulation of the Tkv transcript, which is distributed in a graded fashion complementary to the Dpp gradient (Lecuit and Cohen, 1998) (Fig. S5A). The antibody specifically recognizes Tkv because it: (1) detects a corresponding band of 63 kDa in western blot experiments from developing larvae (not shown); (2) detects overexpression levels of Tkv, induced by the Gal4 system using a *ptc-gal4* driver (Fig. S5B); (3) is titrated out by incubating it, prior to immunostaining, with the peptide used to raise the antibody (Fig. S5C); and (4) does not stain cells lacking Tkv in mutant mosaics (Fig. S5D). In addition, quantitative RT-PCR

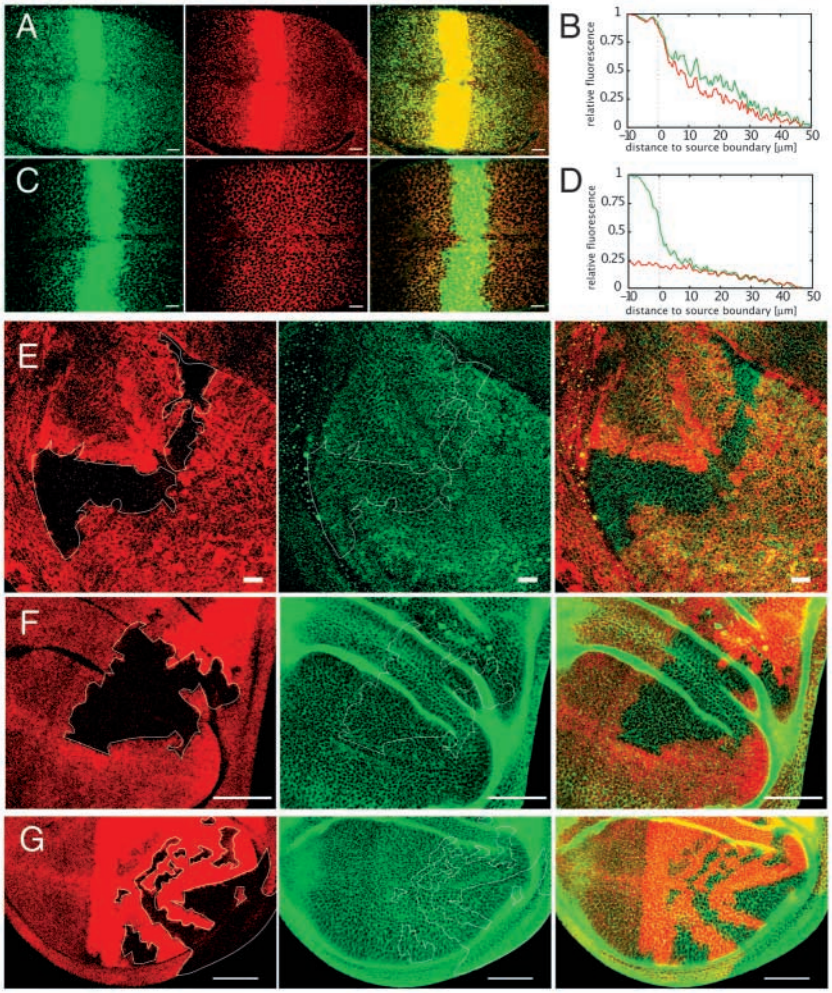

Fig. 5. Extracellular GFP-Dpp and Thickveins localization in *shi^{ts1}* clones. (A,C) Double labelings showing GFP-Dpp distribution (green), total (A) or extracellular (C) GFP immunostaining (red) and overlays. (B,D) Fluorescence intensity profiles of GFP-Dpp (green) and total (B) or extracellular (D) GFP immunostaining (red) in representative discs. Genotype in A-D: *dpp-gal4/UAS-GFP-Dpp*. (E) Double labeling showing *shi^{ts1}* clones after 5 hours at the restrictive temperature (see Materials and methods) marked by the absence of Nmyc (red), and Tkv immunostaining (green). Genotype *shi^{ts1} FRT18A/HS-NM8A FRT18A; HS-Flp/+*. Note that the levels of Tkv outlining the cells are not significantly changed within the mutant mosaics. (F,G) Double labeling showing *shi^{ts1}* clones after 5 hours at the restrictive temperature marked by the absence of DsRed (red) and immunostaining of surface exposed Tkv using the Tkv luminal antibody and the 'extracellular immunostaining protocol' (green; see Materials and methods). Genotype: *shi^{ts1} FRT18A/tub-DsRed FRT18A; HS-Flp/+*. Note that the levels of surface exposed Tkv are not increased within the *shi^{ts1}* mutant clones. White line: clone outline. Scale bars: 10 μm in A-E; 50 μm in F,G.

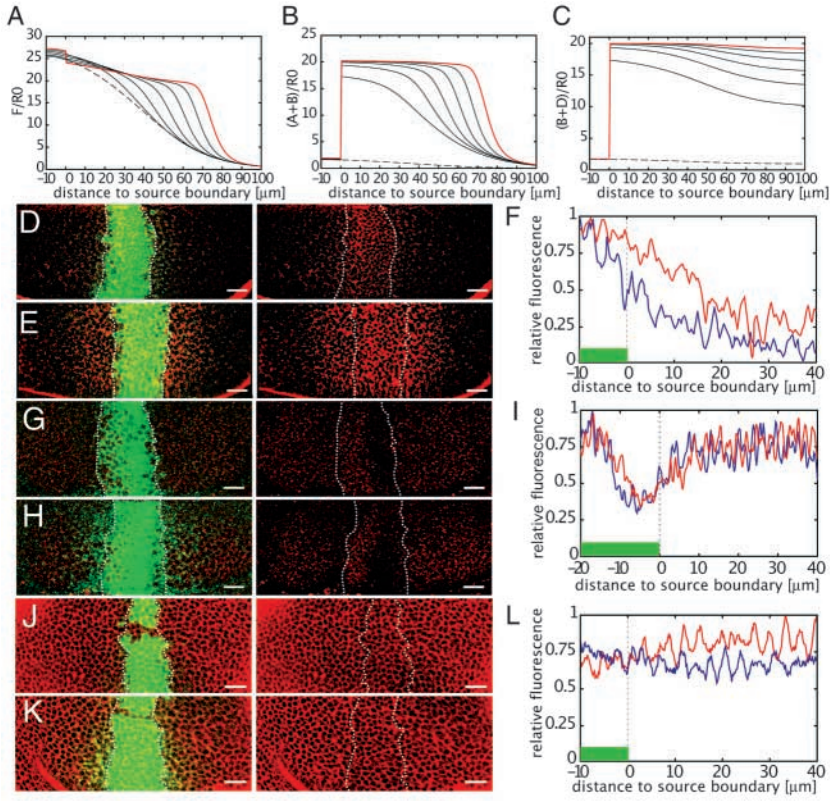

Fig. 6. 'Shibire rescue assay' and the DBTS model. (A-C) Ligand and receptor distributions corresponding to the situation in the 'shibire rescue' experiment calculated in the DBTS model containing a region $-10\ \mu m \leqslant x \leqslant 0\ \mu m$ describing secreting cells. Lines are separated by intervals of 1 hour. At $t=0$, we assume that endocytosis is blocked in the tissue for $x \geqslant 0\ \mu m$. (A) Total ligand concentration $F=A+B+C$. (B) Total extracellular ligand concentration $A+B$, (C) total surface receptor concentration $B+D$. Broken lines indicate the concentrations at $t=0$ given by the steady-state value obtained for parameter values describing a WT tissue. The endocytosis block is modeled by setting the receptor internalization rates to zero for $x \geqslant 0\ \mu m$. The red lines show the concentration after 6 hours, the time at which the experimental observations are made. The calculations are performed in one dimension with an AOI of size $L_x=200\ \mu m$, with 'current boundary conditions' and parameter values as specified in Table 1. (D-I) Extracellular GFP-Dpp and Thickveins localization in the 'shibire rescue' experiment. (D,E) Double labeling showing GFP-Dpp (green) and immunostaining of extracellular GFP-Dpp (red) from a *shi^{ts1}; UAS-Dynamin$^{+/+}$; dpp-gal4/UAS-GFP-Dpp* larva (D) or from a heterozygous *shi^{ts1}*/+ sibling (E) incubated at 34°C for 6 hours. Note that the range of extracellular GFP-Dpp in the hemizygous wing disc is reduced after 6 hours of block at the restrictive temperature. (F) Intensity profiles of extracellular GFP immunostainings in representative discs. Red trace, GFP in a heterozygous sibling. Blue trace, GFP in a hemizygous sibling. Green box, secreting cells. Extracellular GFP-Dpp drops significantly in the receiving tissue when endocytosis is abolished. (G,H) Double labeling showing GFP-Dpp (green) and immunostaining of Tkv (red) from a *shi^{ts1}; UAS-Dynamin$^{+/+}$; dpp-gal4/UAS-GFP-Dpp* larva (G), or from a heterozygous *shi^{ts1}*/+ sibling (H) incubated at 34°C for 6 hours. We also noted a downregulation of Tkv levels of unknown significance abutting the A/P boundary. (I) Intensity profiles of Tkv immunostaining in representative discs. Red trace, Tkv in a heterozygous *shi^{ts1}*/+ sibling. Blue trace, Tkv in a hemizygous *shi^{ts1}* sibling. Tkv-levels do not change in the receiving tissue when endocytosis is abolished for 6 hours. (J,K) Double labeling showing GFP-Dpp (green) and immunostaining of cell surface exposed Tkv using the Tkv luminal antibody and the 'extracellular immunostaining protocol' (red) from a *shi^{ts1}; UAS-Dynamin$^{+/+}$;dpp-gal4/UAS-GFP-Dpp* larva (J), or from a heterozygous *shi^{ts1}*/+ sibling (K) incubated at 34°C for 6 hours. (L) Intensity profiles of cell surface exposed Tkv immunostaining in representative discs. Red trace, Tkv in a heterozygous *shi^{ts1}*/+ sibling. Blue trace, Tkv in a hemizygous *shi^{ts1}* sibling. Surface Tkv levels do not significantly change in the receiving tissue when endocytosis is abolished for 6 hours. In D,E,G,H,J and K broken lines delimit the Dynamin^{+} rescued source. Scale bars: 10 μm.

experiments show that our antibody-staining conditions can robustly detect overexpression levels above 5-fold (Fig. S5B and not shown).

We then addressed whether the levels of surface Tkv are altered in shibire mutant clones when endocytosis is blocked. Fig. 5E shows that in the shibire mutant cells after 5 hours at the restrictive temperature (the experimental conditions that generated the Dpp shadows in the shibire clones), the levels of receptors associated to the cell membranes are not changed. This result indicates that even though endocytosis is blocked during 5 hours, surface receptor levels do not change tenfold or more. To confirm that the Tkv pool associated to the cell profiles correspond to Tkv on the cell surface, we generated an antibody directed against the luminal domain of Tkv (see Materials and methods) and performed the 'extracellular immunostaining' protocol (Strigini and Cohen, 1999). We determined the specificity of this antibody following the same criteria discussed above (Fig. S5E-G). As with the other Tkv antibody, our antibody staining in this condition can robustly detect overexpression levels above 5-fold (Fig. S5), as monitored by RT-PCR (not shown). Figs 5F,G show that the levels of surface Tkv are not affected upon 5 hours of endocytic block in the shibire mutant clones. The observed shadow can therefore not result from a mechanism based on a high surface Tkv receptor concentration as in the DBT and DBTS models.

According to the DBT model, the levels of internalized Dpp are significantly increased inside the clone after long time periods (Fig. 7C,D). This may seem surprising when internalization is blocked. The effect is because decreased internalization by a factor of 10 leads to an accumulation of the surface receptors, which in turn increases the levels of receptor-mediated endocytosis of Dpp. Such an effect was not observed inside the shibire clone in which the levels of intracellular Dpp were reduced after 5 hours (M.G.-G., unpublished) (Entchev et al., 2000). A reduced internal Dpp concentration is achieved in the DBTS model if the internalization rates inside the clone are set to zero (Fig. 7E, Fig. 4C, inset). Furthermore, in the DBT model, the total concentration of ligand inside the clone is significantly higher as compared with outside the clone (Fig. 7B).

Finally, note that both for the DBT (Fig. 3C, inset) and the DBTS model (not shown), the extracellular level of ligand is

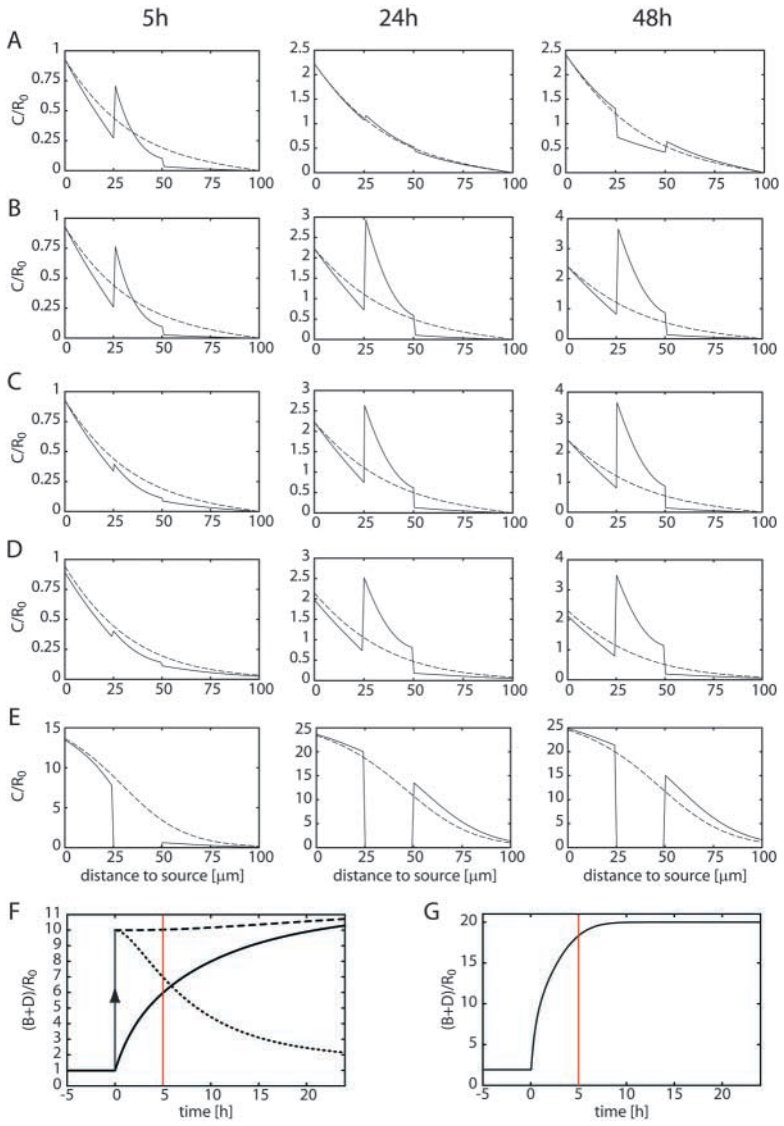

Fig. 7. Concentrations of internal-bound ligand (*C*) in the presence of a *shi*^{ts1} clone calculated in the DBT and the DBTS models. (A) Replication of the one-dimensional calculations of Lander et al. (Lander et al., 2002) for the DBT model. Profiles of internal-bound ligand at 5 hours, 24 hours, and 48 hours obtained for the same parameters as in Lander et al. (Lander et al., 2002) (see Table 1) with 'concentration boundary conditions' and L_x=100 μm. The endocytic block in the clone is described by a tenfold reduction of receptor internalization rates (k_p, k_{in}). In addition, at time t=0, the surface receptor concentration was suddenly increased by a factor of 10 inside the clone as described in Lander et al. (Lander et al., 2002). Note, that in order to replicate the results shown in Fig. 7 of Lander et al. (Lander et al., 2002), the receptor production rate w had also to be reduced by a factor of 10. After 5 hours the ligand concentration is reduced behind the clone as compared with the results of the same calculation in the absence of a clone (broken line). This corresponds to a shadow in the experiments. At 24 hours, the shadow is weak. This is not a steady state situation because after 48 hours, an accumulation of ligand behind the clone and depletion in the clone occur. (B) One-dimensional calculation as described in A, but with correct receptor production rate w in the clone region (not reduced by a factor of 10). A shadow builds up which increases in time and persists. (C) One-dimensional calculation as in B (i.e. corrected w), but further corrected with surface receptor concentration in the clone region which increases gradually according to the DBT model (see also Fig. 3). (D) Distribution of internal-bound ligand in a two-dimensional calculation for the DBT model with L_x=200 μm and L_y=200 μm at 5 hours, 24 hours, and 48 hours along a section through the clone in x-direction, as in Fig. 3C (unbroken line) and Fig. 3D (broken line). Note that the one-dimensional and two-dimensional calculations generate similar profiles for the geometry of area of interest (AOI) and clone size chosen (compare C and D). Note also that in both cases there is a shadow that persists in the steady state. (E) Ligand distributions as described in D, but obtained for the DBTS model for saturating surface receptors and zero internalization rates. A shadow is present at 5 hours and has disappeared at 24 hours. There is no internal-bound ligand inside the clone. In A-E, the clone extends from x=25 μm to x=50 μm. (F) Total surface receptor concentration, $B+D$, in the center of the clone. The dotted line corresponds to the calculation shown in A, the broken line to B, and the unbroken line to the calculation shown in D (a similar profile corresponds to C). (G) Total surface receptor concentration, $B+D$, in the center of the clone for the calculation shown in E.

significantly increased in the clone. Such an extracellular accumulation of Dpp was not observed (Entchev et al., 2000).

Both DBT and DBTS models are inconsistent with the observed ligand and receptor concentrations in the 'shibire rescue assay'

The 'shibire rescue assay' allows us to monitor how blocking endocytosis in the receiving cells has an effect on the formation of the Dpp gradient and on the levels of intracellular and extracellular ligand and receptor (Entchev et al., 2000). In these experiments, the receiving cells cannot perform endocytosis at the restrictive temperature in a *shibire* mutant animal, whereas the secreting cells are rescued with a *Dynamin*$^+$ transgene and can thereby perform endocytosis normally (see Materials and methods). At the permissive temperature, a GFP-Dpp gradient forms in the target tissue. After a temperature shift to the restrictive temperature, endocytosis is blocked in the receiving cells. Upon 6 hours of endocytic block, internalized Dpp has disappeared and no gradient can be observed (Entchev et al., 2000).

We use the DBTS model to calculate ligand profiles under conditions that correspond to this shibire rescue experiment. We modify the AOI and include a region with –10 μm<x<0 representing half of the stripe of producing cells (Fig. 2C). This region is described by the DBTS model with the same parameters as before, but in addition each cell in this region also secretes ligand with rate v. Because of the symmetry of the source, we now impose zero ligand current as a boundary condition at x=–10 μm (see supplementary material). In WT, endocytosis is active and the ligand-concentration profiles (Fig. 6A, broken line) closely resemble those obtained without explicitly describing the source (Fig. 2D).

At the permissive temperature, the gradients of extracellular ligand generated by the DBTS model (Fig. 6B, broken line) are

consistent with the observed levels of extracellular Dpp in WT (Fig. 5D) and in the control discs of the 'shibire rescue' experiment (Fig. 6E,F). In the source, we observed a large accumulation of GFP-Dpp, probably corresponding to ligand in the secretory pathway (Fig. 6D,E,G,H,J,K). This pool of Dpp is not included in our model.

After 6 hours of endocytic block in the 'shibire rescue' discs (modeled by setting the internalization rates in the target tissue to zero), the calculated total (Fig. 6A, red line) and extracellular ligand (Fig. 6B, red line) distributions in the DBTS model changes by a factor of up to four (total) and up to ten (extracellular) in the receiving tissue and generate a long-range gradient of high levels of Dpp. In contrast, when we monitor total and extracellular Dpp after 6 hours of the endocytotic block at the restrictive temperature in the experiments, the Dpp concentration decreases and the range of the extracellular Dpp gradient is reduced (Fig. 6D-F) (Entchev et al., 2000). Notably, whereas the DBTS model exhibits a discontinuous behavior of the external ligand concentration between the WT source and the receiving tissue with blocked endocytosis (Fig. 6B), no such discontinuity is observed in the experiment (Fig. 6D-F).

We also investigated the surface receptor levels in the 'shibire rescue assay'. The DBTS model generates a discontinuity of the levels of surface receptors by a factor of 20 in the receiving cells when compared with the source after 6 hours of the endocytic block (Fig. 6C, red line). To monitor the surface receptor levels, we performed Tkv immunostainings in the 'shibire rescue' discs after endocytic block. No significant increase in the receptor levels between the WT source and the receiving cells could be found (Fig. 6G-I). Furthermore, the levels of surface Tkv were not increased in the mutant cells as determined by 'extracellular immunostaining' (Strigini and Cohen, 1999) using the antibody directed against the Tkv luminal domain (Fig. 6J-L).

The 'shibire rescue assay' was compared with results of the DBTS model. The distributions of both the extracellular ligand and the surface receptor densities remain qualitatively the same in the DBT model as in the DBTS model (not shown). Our comparison of experiment and theory therefore leads to the conclusion that high surface receptor levels cannot be the origin of the shadows in the 'shibire shadow assay'.

Discussion

In this report, we have studied whether ligand transport by extracellular diffusion can explain the spreading of Dpp through the target tissue. We compared the theoretical results of two models, in which transport is exclusively because of extracellular diffusion of the ligand, with a direct measurement of the extracellular and intracellular pool of ligand as well as the levels of total and cell surface receptor in WT and in endocytosis-defective mosaic tissues. The current models in which ligand transport is solely because of free extracellular diffusion are inconsistent with the experimental results obtained by the 'shibire shadow assay' and the 'shibire rescue assay'.

Three points lead to this conclusion. First, a DBT model of the 'shibire shadow assay' generates permanent shadows (Figs 3, 7), whereas the experimental shadows are transient (Entchev et al., 2000). Second, the DBTS model can generate transient shadows, but only if the surface receptor levels in the clone increase dramatically (Fig. 4). This leads to a strong increase in the levels of extracellular ligand in the clone (Fig. 4C). Using receptor antibodies in the 'shibire shadow assay', we did not observe these higher levels of surface receptors in the clone (Fig. 5E-G). Similarly, the levels of extracellular ligand were not increased in the clone (Entchev et al., 2000). Third, in the DBTS model for the 'shibire rescue assay', the levels of both the extracellular Dpp and the surface receptors are dramatically increased in the endocytosis-defective target cells as compared with the WT source (Fig. 6B,C). Such an increase is not seen experimentally (Fig. 6D,G). Instead, extracellular Dpp enters the receiving tissue over a distance of only 4-5 cells in steady-state (Fig. 6D,F). This is in contrast to both DBT and DBTS models of the 'shibire rescue assay' in which ligand can enter the tissue over large distances. Therefore, in addition to downregulating surface receptors, endocytosis is likely to play additional roles in the transport of ligands during gradient formation.

These three caveats of the DBT/DBTS models are actually not caused by the choice of a particular set of parameters. The parameter values used in our calculations (Table 1) were chosen in such a way, that the typical distance over which the ligand gradient extends as well as the characteristic time to reach steady state are consistent with the experimentally observed profiles. Furthermore, if possible, parameters were chosen similar to values measured for the EGF receptor in a cell culture system (Table 1). In the case of the DBT model they are the same parameters used in Lander et al. (Lander et al., 2002) when they studied the diffusion model. Note that our results showing that a high surface receptor concentration inside the clone is required for shadows to appear is independent of any choice of parameters. Furthermore, convincing shadows appear in the DBT and DBTS models only for values of k_{off}, which are small compared with those typically measured in related systems (Table 1). It will be necessary to estimate the actual parameter values for Dpp during wing morphogenesis in order to ultimately understand its mechanism of spreading (see below).

Models for morphogen transport: importance of dimensions, AOI size and boundary conditions

The geometry and boundary conditions discussed here differ from those introduced in Lander et al. (Lander et al., 2002). There, the one-dimensional case is considered exclusively, i.e. concentrations of ligand and receptor that are independent of y, even in the presence of a clone. At the boundaries $x=0$ and $x=L_x$, Lander et al. imposed the ligand concentrations. In particular, at $x=L_x$ the concentration was fixed to $A=0$, which implies that all ligands that reach $x=L_x$ are instantaneously degraded. Such a Dpp sink does not exist in the wing disc. This sink has a significant influence on the shape of the gradient obtained in the calculations of Lander et al., with $L_x=100$ μm, whereas the difference becomes insignificant for $L_x=200$ μm (see Fig. S3C,D in the supplementary material).

At $x=0$, the boundary conditions imposed by Lander et al. are also problematic. These boundary conditions imply that at $x=0$ the ligand concentration is imposed by the secreting cells but is unaffected by the exchange of ligands between secreting and non-secreting cells via diffusion (for details, see supplementary material). We refer to the boundary conditions

imposing the ligand concentration and the ligand current as ‘concentration boundary conditions’ (Lander et al., 2002) and ‘current boundary conditions’ (this work), respectively.

We also performed one-dimensional calculations in the presence of a clone (Fig. 7A-C). In these calculations, the clone region is represented by an interval on the *x*-axis. We find that a one-dimensional description can generate ligand profiles that qualitatively correspond to the profiles in the *x*-direction of a two-dimensional calculation (Fig. 3C), if the extension of the clone in the *y*-direction is larger than the distance over which the gradient forms (compare Fig. 7C and 7D). For the present choice of parameters and an extension of the clone of 50 μm in *y*-direction, this criterion is satisfied. The contrast *c* of shadows in the two-dimensional geometry can be determined approximately in a one-dimensional calculation by taking the difference of the concentration behind the clone and the concentration at the same position in a calculation without a clone. In general, however, a two-dimensional description is required to describe the effects of the clone.

Transient versus permanent shadows

Our results show that the DBT model generates permanent shadows behind the clone, whereas a DBTS model is able to generate transient shadows similar to those observed in the experiments by Entchev et al. (Entchev et al., 2000). Note, that this finding differs from the results of Lander et al. (Lander et al., 2002), who concluded that the DBT model can generate transient shadows.

In their one-dimensional calculations of the DBT model, like in ours, endocytosis block is modeled by a tenfold reduction of the internalization rates at t=0. However, in their study, the receptor concentrations $[R_{out}]$ and $[R_{in}]$ in the clone are simultaneously and abruptly set to the steady-state values corresponding to the reduced internalization rates. This assumption does not correspond to the experimental situation interpreted in the framework of the DBT model, because it would imply an instantaneous tenfold increase of the surface receptor concentration within the clone at the time of the temperature shift (see broken line in Fig. 7F). This is different from what is expected to happen in the experiment according to the DBT model: as the internalization rates in the clone are reduced in an abrupt fashion at t=0, the concentration of surface receptors only gradually increases (Fig. 7F, unbroken line). We have performed the same calculations as described in Lander et al., but changing the initial conditions for the receptor concentration (Fig. 7C). This one-dimensional calculation qualitatively leads to the same result as already discussed in two dimensions: a shadow develops that at t=5 hours is weak and becomes more pronounced after long time periods (compare Fig. 7C and 7D).

We have repeated the calculations of Lander et al., using the parameter values and system size, the boundary conditions, and the initial conditions chosen in their article. Note that in these calculations, we have set the initial surface receptor concentration in the clone to a tenfold larger value as compared with the remaining tissue as discussed above. As a result, we obtain ligand profiles that after long time periods exhibit a persistent shadow in the steady state identical to the situation in which the surface receptor level increases gradually (compare Fig. 7B and 7C). We found no transient shadows in these calculations. This result is different from the one published in their work (Fig. 7B).

The fact that these calculations lead to ligand profiles that differ from those published in Lander et al. (Lander et al., 2002) indicates a possible technical problem in their calculations. Repeating the calculations of Lander et al., we noticed that their results could be reproduced. However, this was possible only if the receptor production rate inside the clone was reduced by a factor of 10 at t=0 as compared with the one outside the clone. The results of our calculations with this additional change in the clone are displayed in Fig. 7A. In this case, the surface receptor concentration in the clone after undergoing an initial step-wise increase, relaxes to a steady-state value that is similar to the steady state in the tissue outside the clone (Fig. 7F, dotted line). The corresponding ligand profiles of Fig. 7A indeed coincide with the results published in Lander et al. (Lander et al., 2002), see Fig. 7 therein. It is possible that in these calculations the receptor production rate in the clone was reduced by a factor of 10. In summary, in the case of the calculations discussed in Lander et al. (Lander et al., 2002), the shadow most likely appears because of the sudden step-wise increase of the surface receptor level; the shadow disappears at 24 hours because the receptor production rate is reduced and the surface receptor level therefore relaxes to approximately the same steady state as outside the clone.

Our results emphasize the facts that the number of dimensions considered (in particular in the presence of mutant clone) (Figs 3, 4), the size of the AOI (see Fig. S3 in the supplementary material), the boundary conditions (in particular the ‘source boundary’ and the ‘distal boundary’) (Fig. 2), and the initial conditions (most notably the levels of surface receptor in the clone at the beginning of the experiment) (Fig. 7F) are of key importance.

Why the DBT/DBTS models fail to explain Dpp spreading

We have shown in this work that neither the DBT nor the DBTS model can explain the observed ligand and receptor profiles during Dpp spreading in the wing disc. Why should these models fail even though they incorporate many essential phenomena such as ligand diffusion, internalization and resurfacing via receptor recycling?

The essential point of both the DBT and the DBTS model is that ligand transport, which is described by the ligand current given in Eqn 1, is solely because of diffusion. In other words, this means that ligand bound to the surface receptors when internalized can only resurface at the same position on the cell surface where it was internalized. Only in this case is Eqn 1 justified and the intracellular transport of the ligand would not contribute to the current of the ligand in the tissue. This implies that simple reaction diffusion models ignore that in principle, ligand could also be transported by traveling through cells and resurface at other positions on the cell surface when receptors are recycled.

The fact that the DBT and DBTS models, which ignore these effects, cannot account for observed Dpp spreading suggests that contributions of receptor trafficking to transport and ligand current may indeed play an important role. We are currently generalizing the DBT/DBTS models to incorporate all relevant transport phenomena (diffusion and transcytosis) in the ligand

current as well as the possibility of extracellular degradation of the ligand.

Interplay of diffusion and planar transcytosis: a working hypothesis for Dpp spreading

Our working hypothesis is that two phenomena contribute to the Dpp current in the developing wing epithelium: extracellular diffusion and intracellular trafficking (i.e. endocytosis plus resecretion). What is the relative importance of these two phenomena to the spreading of the morphogen? Both might be important. Limited by binding to the extracellular matrix and/or degradation, extracellular transport of the morphogen may only account for the spreading of the ligand across a few cell diameters. Intracellular trafficking in turn accounts for the movement of the morphogen across one cell diameter. Both phenomena together then lead to the long-range spreading of the morphogen.

Although it is expected that extracellular diffusion plays a role during morphogen spreading (Crick, 1970), it has been argued that extracellular diffusion alone is insufficient to understand the reliability and precision of the formed gradient (Kerszberg and Wolpert, 1998). The important role of intracellular trafficking has been uncovered in experiments in which endocytosis is blocked during morphogenetic signaling (González-Gaitán, 2003). When endocytosis is blocked in the receiving tissue, Dpp spreading does occur, but generates a short-range gradient and thereby signaling responses only within 3 to 5 cells (Entchev et al., 2000; González-Gaitán and Jäckle, 1999). In particular, in a thermosensitive alpha-adaptin mutant, Dpp activates transcription of its target gene *spalt* only within 4-5 cells from the source (González-Gaitán and Jäckle, 1999), instead of within 15 cells in WT. Similar results where obtained by expressing a dominant-negative Rab5 mutant, which impairs endocytosis and endosomal dynamics (Entchev et al., 2000). These results do not exclude a role of endocytosis in the transduction, rather than on the spreading of Dpp. However, in the 'shibire rescue assay', the reduced range of the extracellular Dpp gradient (Fig. 6D,E) indicates that impaired endocytosis restricts the spreading of Dpp.

This report is a theoretical and experimental study to address whether diffusion as the sole transport mechanism can explain the spreading of Dpp. We are currently studying the role of different transport mechanisms for Dpp spreading. Based on the values given in Table 1, it has been argued that the rates of endocytosis and recycling known for the EGF receptor in cultured cells are too small to allow for a sufficiently rapid transport by transcytosis (Lander et al., 2002). Indeed, our first results based on generalized models (including diffusion and transport by planar transcytosis) show that the parameter values used in this work (Table 1) do not produce consistent gradients during reasonable times. In particular, these models require a faster rate of endocytosis and recycling than those known for the EGF receptor in cultured cells. Therefore, it is essential to measure directly the different dynamic parameters, including the extracellular diffusion coefficient as well as the rates of endocytosis, degradation and recycling of Dpp in the developing wing. To estimate these parameters in situ we are currently monitoring photoactivatable fusion proteins in different cellular locations (extracellular versus endosomal) in the very context of the developing wing epithelium.

We thank A. Schwabedissen and D. Backasch for their excellent technical assistance. T. Lecuit, K. Simons, D. Lubensky, K. Sekimoto and people in the González laboratory for comments on the manuscript. This work was supported by the Max Planck Society and Deutsche Forschungsgemeinschaft.

Supplementary material

Supplementary material for this article is available at
http://dev.biologists.org/cgi/content/full/131/19/4843/DC1

References

Alberts, B., Bray, D., Lewis, J., Raff, M., Roberts, K. and Watson, J. D. (1994). *Molecular Biology of the Cell*. NY: Garland Publisher.

Basler, K. and Struhl, G. (1994). Compartment boundaries and the control of *Drosophila* limb pattern by Hedgehog protein. *Nature* **368**, 208-214.

Chen, M. S., Obar, R. A., Schroeder, C. C., Austin, T. W., Poodry, C. A., Wadsworth, S. C. and Vallee, R. B. (1991). Multiple forms of Dynamin are encoded by *shibire*, a *Drosophila* gene involved in endocytosis. *Nature* **351**, 583-586.

Chu, L., Wiley, H. S. and Lauffenburger, D. A. (1996). Endocytic relay as a potential means for enhancing ligand transport through cellular tissue matrices: analysis and possible implications for drug delivery. *Tissue Eng.* **2**, 17-38.

Crick, F. (1970). Diffusion in embryogenesis. *Nature* **225**, 420-422.

Eldar, A., Dorfman, R., Weiss, D., Ashe, H., Shilo, B. Z. and Barkai, N. (2002). Robustness of the BMP morphogen gradient in *Drosophila* embryonic patterning. *Nature* **419**, 304-308.

Eldar, A., Rosin, D., Shilo, B. Z. and Barkai, N. (2003). Self-enhanced ligand degradation underlies robustness of morphogen gradients. *Dev. Cell* **5**, 635-646.

Entchev, E. V., Schwabedissen, A. and González-Gaitán, M. (2000). Gradient formation of the TGF-beta homolog Dpp. *Cell* **103**, 981-991.

Gierer, A. (1981). Generation of biological patterns and form: some physical, mathematical, and logical aspects. *Prog. Biophys. Mol. Biol.* **37**, 1-47.

Gierer, A. and Meinhardt, H. (1972). A theory of biological pattern formation. *Kybernetik* **12**, 30-39.

González-Gaitán, M. (2003). Signal dispersal and transduction through the endocytic pathway. *Nat. Rev. Mol. Cell. Biol.* **4**, 213-224.

González-Gaitán, M. A. and Jäckle, H. (1999). The range of *spalt*-activating Dpp signalling is reduced in endocytosis-defective *Drosophila* wing discs. *Mech. Dev.* **87**, 143-151.

Harsay, E. and Schekman, R. (2002). A subset of yeast vacuolar protein sorting mutants is blocked in one branch of the exocytic pathway. *J. Cell Biol.* **156**, 271-285.

Herbst, J. J., Opresko, L. K., Walsh, B. J., Lauffenburger, D. A. and Wiley, H. S. (1994). Regulation of postendocytic trafficking of the epidermal growth factor receptor through endosomal retention. *J. Biol. Chem.* **269**, 12865-12873.

Houchmandzadeh, B., Wieschaus, E. and Leibler, S. (2002). Establishment of developmental precision and proportions in the early *Drosophila* embryo. *Nature* **415**, 798-802.

Kerszberg, M. and Wolpert, L. (1998). Mechanisms for positional signalling by morphogen transport: a theoretical study. *J. Theor. Biol.* **191**, 103-114.

Koch, A. J. and Meinhardt, H. (1994). Biological pattern-formation – from basic mechanisms to complex structures. *Rev. Mod. Phys.* **66**, 1481-1507.

Lander, A. D., Nie, Q. and Wan, F. Y. (2002). Do morphogen gradients arise by diffusion? *Dev. Cell* **2**, 785-796.

Lauffenburger, D. A. and Linderman, J. J. (1993). Receptors: models for binding, trafficking, and signalling. NY: Oxford University Press.

Lecuit, T. and Cohen, S. M. (1998). Dpp receptor levels contribute to shaping the Dpp morphogen gradient in the *Drosophila* wing imaginal disc. *Development* **125**, 4901-4907.

Nellen, D., Affolter, M. and Basler, K. (1994). Receptor serine/threonine kinases implicated in the control of the *Drosophila* body pattern by decapentaplegic. *Cell* **78**, 225-237.

Nellen, N., Burke, R., Struhl, G. and Basler, K. (1996). Direct and long-range action of a DPP morphogen gradient. *Cell* **85**, 357-368.

Ramaswami, M., Krishnan, K. S. and Kelly, R. B. (1994). Intermediates in

synaptic vesicle recycling revealed by optical imaging of *Drosophila* neuromuscular junctions. *Neuron* **13**, 363-375.

Starbuck, C. and Lauffenburger, D. A. (1992). Mathematical model for the effects of epidermal growth factor receptor trafficking dynamics on fibroblast proliferation responses. *Biotechnol. Prog.* **8**, 132-143.

Strigini, M. and Cohen, S. M. (1999). Formation of morphogen gradients in the *Drosophila* wing. *Semin. Cell. Dev. Biol.* **10**, 335-344.

Strigini, M. and Cohen, S. M. (2000). Wingless gradient formation in the *Drosophila* wing. *Curr. Biol.* **10**, 293-300.

Tabata, T. (2001). Genetics of morphogen gradients. *Nat. Rev. Genet.* **2**, 620-630.

Teleman, A. A. and Cohen, S. M. (2000). Dpp gradient formation in the *Drosophila* wing imaginal disc. *Cell* **103**, 971-980.

Turing, A. M. (1952). The chemical basis of morphogenesis. *Philos. Trans. R. Soc. London* **237**, 37-72.

Verstreken, P., Kjaerulff, O., Lloyd, T. E., Atkinson, R., Zhou, Y., Meinertzhagen, I. A. and Bellen, H. J. (2002). Endophilin mutations block clathrin-mediated endocytosis but not neurotransmitter release. *Cell* **109**, 101-112.

Vincent, J. P. and Dubois, L. (2002). Morphogen transport along epithelia, an integrated trafficking problem. *Dev. Cell* **3**, 615-623.

Wolpert, L. (1969). Positional information and the spatial pattern of cellular differentiation. *J. Theor. Biol.* **25**, 1-47.

Xu, T. and Harrison, S. D. (1994). Mosaic analysis using FLP recombinase. In *Drosophila Melanogaster: Practical Uses in Cell and Molecular Biology* (ed. E. A. Fyrberg), pp. 655-681. San Diego, CA: Academic Press.

Dpp gradient formation by dynamin-dependent endocytosis: receptor trafficking and the diffusion model

- Supplementary Material -

Karsten Kruse*,[1] Periklis Pantazis*,[2] Tobias Bollenbach,[1]
Frank Jülicher,[1] and Marcos González-Gaitán[2]

[1]*Max-Planck-Institut for Physics of Complex Systems, Nöthnitzer Str. 38, 01187 Dresden, Germany*

[2]*Max-Planck-Institut for Molecular Cell Biology and Genetics, Pfotenhauer Str. 108, 01307 Dresden, Germany*

* These authors contributed equally to this work.

In the following we explicitly present the scheme used to integrate the dynamic equations of the DBT and the DBTS model, study the effects of different AOI sizes on morphogen gradients, and present equations describing the dynamics of GFP-Dpp in the presence of endogenous Dpp as well as equations incorporating the standard biosynthetic pathway for surface receptor production.

THE DYNAMIC EQUATIONS OF THE DBT AND THE DBTS MODEL

For convenience we summarize in the following the dynamic equations for the DBT and the DBTS model. The DBT model is given by:

$$\frac{\partial}{\partial t}A = D_0(\frac{\partial^2}{\partial x^2} + \frac{\partial^2}{\partial y^2})A - k_{\rm on}AD + k_{\rm off}B \tag{1}$$

$$\frac{\partial}{\partial t}B = k_{\rm on}AD - (k_{\rm in} + k_{\rm off})B + k_{\rm out}C \tag{2}$$

$$\frac{\partial}{\partial t}C = k_{\rm in}B - (k_{\rm out} + k_{\rm deg})C \tag{3}$$

$$\frac{\partial}{\partial t}D = k_{\rm off}B + k_qE - k_{\rm on}AD - k_pD \tag{4}$$

$$\frac{\partial}{\partial t}E = w + k_pD - (k_q + k_g)E \tag{5}$$

Here, $A = [L]_{\rm out}$ is the concentration of free extracellular ligands, $B = [LR]_{\rm out}$ is the concentration of ligand bound receptors on cell surfaces, $C = [LR]_{\rm in}$ is the concentration of ligand bound receptors inside cells, $D = [R]_{\rm out}$ and $E = [R]_{\rm in}$ are the concentrations of free receptors outside and inside the cell, respectively. The diffusion term can be written as the divergence of a current $\mathbf{J}$:

$$D_0(\frac{\partial^2}{\partial x^2} + \frac{\partial^2}{\partial y^2})A = -\frac{\partial}{\partial x}J_x - \frac{\partial}{\partial y}J_y \quad , \tag{6}$$

with

$$\mathbf{J} = (J_x, J_y) = -D_0(\frac{\partial}{\partial x}A, \frac{\partial}{\partial y}A) \quad . \tag{7}$$

In the DBTS model, the surface receptor concentration saturates at a maximal density $R_{\max}$. The corresponding dynamic equations read:

$$\frac{\partial}{\partial t}A = D_0(\frac{\partial^2}{\partial x^2} + \frac{\partial^2}{\partial y^2})A - k_{\rm on}AD + k_{\rm off}B \tag{8}$$

$$\frac{\partial}{\partial t}B = k_{\rm on}AD - (k_{\rm in} + k_{\rm off})\,B + k^0_{\rm out}\left(1 - \frac{B+D}{R_{\max}}\right)C \tag{9}$$

$$\frac{\partial}{\partial t}C = k_{\rm in}B - \left(k^0_{\rm out}\left(1 - \frac{B+D}{R_{\max}}\right) + k_{\rm deg}\right)C \tag{10}$$

$$\frac{\partial}{\partial t}D = k_{\rm off}B + k^0_q\left(1 - \frac{B+D}{R_{\max}}\right)E - k_{\rm on}AD - k_pD \tag{11}$$

$$\frac{\partial}{\partial t}E = w + k_pD - \left(k^0_q\left(1 - \frac{B+D}{R_{\max}}\right) + k_g\right)E \tag{12}$$

Receptor production

In the DBT and the DBTS model, the receptor production rate w appears in the equation for the distribution E of free internal receptors. This reflects the appearance of newly formed receptor molecules in endosomes. The conventional biosynthetic pathway, however, does not involve endosomal structures [1], see Fig. 2B . Instead receptors formed *de novo* appear directly on the cell surface. This can be incorporated into the DBT and DBTS model by modifying the dynamic equations for the distributions of free internal and free surface receptors. Explicitly, for the DBT model, we replace Eqs. (4) and (5) by

$$\frac{\partial}{\partial t}D = w + k_{\rm off}B + k_qE - k_{\rm on}AD - k_pD \tag{13}$$

$$\frac{\partial}{\partial t}E = k_pD - (k_q + k_g)E \quad . \tag{14}$$

For the DBTS model Eqs. (11) and (12) are replaced by

$$\frac{\partial}{\partial t}D = w^0\left(1 - \frac{B+D}{R_{\max}}\right) + k_{\rm off}B + k^0_q\left(1 - \frac{B+D}{R_{\max}}\right)E - k_{\rm on}AD - k_pD \tag{15}$$

$$\frac{\partial}{\partial t}E = k_pD - (k^0_q\left(1 - \frac{B+D}{R_{\max}}\right) + k_g)E \quad . \tag{16}$$

Numerical solutions of the modified models show only a minor effect of this change on the dynamics, see Fig. S1.

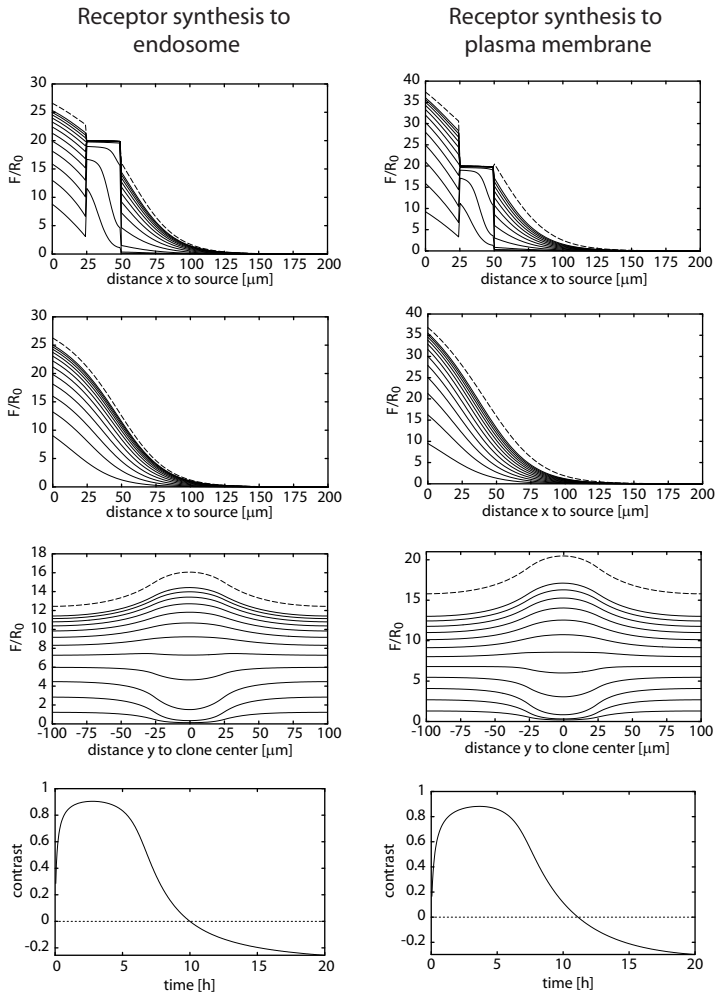

Figure S1. Receptor synthesis in the DBTS model. Total ligand profiles obtained from a two-dimensional calculation of the DBTS model with receptor synthesis directed to the plasma membrane according to Eqs. (15) and (16) compared to those obtained from the calculation shown in Fig. 4. For the calculation shown on the right, the rate of receptor synthesis w was modified just like k_q and k_{out} to obtain cell surface receptor saturation. Note, that $R_0 = w^0(1 + k_q/k_g)/k_p$ in the calculation on the right. Otherwise the same parameters as for the DBTS model calculation described in the paper were used. The initial conditions for the calcualtion on the right were $A = B = C = 0$, $D = R_0$, and $E = k_p R_0/(k_g + k_q)$.

NUMERICAL SOLUTION OF THE DYNAMIC EQUATIONS

We numerically solve the dynamic equations by using the Euler discretization forward in time. In the forward Euler scheme, the partial derivatives in space and time of a function f are approximated by

$$\frac{\partial}{\partial x} f(x,t) = \frac{f(x+\Delta x,t)-f(x,t)}{\Delta x} \tag{17}$$

$$\frac{\partial}{\partial t} f(x,t) = \frac{f(x,t+\Delta t)-f(x,t)}{\Delta t} \quad . \tag{18}$$

$$\tag{19}$$

We now explicitly describe the discretization scheme, first for the dynamics in the bulk, then for the dynamics at the boundaries.

Bulk dynamics

One dimension

Consider a system that is homogenous in the y-direction. Then only the dynamics in the x-direction has to be determined and we are left with a one dimensional system. In order to describe the area of interest (AOI), we introduce a one-dimensional lattice of size N with the sites being separated by a distance Δx. The ligand and receptor distributions are sampled on the sites. We define $A_n := A(n\Delta x, t)$, where $n = 0, \ldots, N = L/\Delta x$, and correspondingly B_n, C_n, D_n, and E_n. Primed quantities denote the distributions at time $t + \Delta t$, e.g., $A'_n := A(n\Delta x, t + \Delta t)$. In the bulk, i.e., for $n = 1, \ldots, N-1$, the discretization of the dynamic equations is then given by

$$A'_n = A_n + \Delta t \left[\frac{j_n - j_{n+1}}{\Delta x} - k_{\text{on}} A_n D_n + k_{\text{off}} B_n \right] \tag{20}$$

$$B'_n = B_n + \Delta t \left[k_{\text{on}} A_n D_n - (k_{\text{in}} + k_{\text{off}}) B_n + k_{\text{out}} C_n \right] \tag{21}$$

$$C'_n = C_n + \Delta t \left[k_{\text{in}} B_n - (k_{\text{out}} + k_{\text{deg}}) C_n \right] \tag{22}$$

$$D'_n = D_n + \Delta t \left[k_{\text{off}} B_n + k_q E_n - k_{\text{on}} A_n D_n - k_p D_n \right] \tag{23}$$

$$E'_n = E_n + \Delta t \left[w + k_p D_n - (k_q + k_g) E_n \right] \quad . \tag{24}$$

Here,

$$j_n = -\frac{D_0}{\Delta x}(A_n - A_{n-1}) \quad . \tag{25}$$

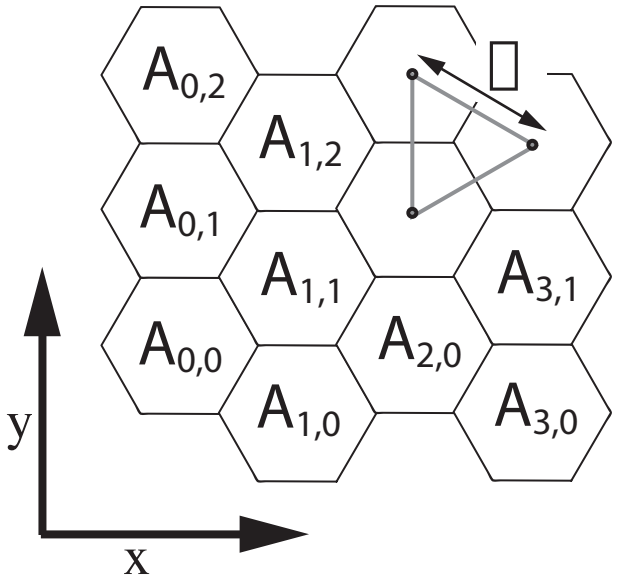

Figure S2. Illustration of the discretization scheme used for the numerical calculations in two dimensions. Sites are arranged on a triangular lattice and are separated by a distance Δ. The sites are indexed by (n, m). The first component of the index gives the position in x-direction, the second component in y-direction where $n = 0, \ldots, N = L_x/\sqrt{3}\Delta$ and $m = 0, \ldots, M = 2L_y/\Delta$.

Two dimensions

In the two-dimensional case, the discretization sites in the AOI are arranged on a triangular lattice with lattice constant Δ, which is the distance between two neighbouring sites, see Fig. S2. The sites can be indexed by two indices n and m, where $n = 0, \ldots, N = L_x/\sqrt{3}\Delta$ and $m = 0, \ldots, M = 2L_y/\Delta$, see Fig. S2. Explicitly,

$$A_{n,m} = \begin{cases} A(n\sqrt{3}\Delta/2, m\Delta) & \text{for} \quad n \text{ even} \\ A(n\sqrt{3}\Delta/2, (m-1/2)\Delta) & \text{for} \quad n \text{ odd} \end{cases} \quad . \tag{26}$$

The other densities are discretized correspondingly. The terms in Eqs. (20)-(24) describing ligand binding to and unbinding from receptors are readily modified to this situation. The current from site $(\bar{n}, \bar{m})$ to a neighbouring site (n, m) is proportional to $-(A_{\bar{n},\bar{m}} - A_{m,n})/\Delta$ and the discretization of the diffusion term reads

$$\frac{2D_0}{3\Delta^2} \sum_{\langle \bar{m},\bar{n} \rangle} (A_{\bar{n},\bar{m}} - A_{n,m}) \quad . \tag{27}$$

Here, the sum over the sites $(\bar{n}, \bar{m})$ extends over all nearest neighbours of the site (n, m).

Dynamics at the boundaries

We will describe the treatment of the boundary terms only for the one-dimensional case; the two-dimensional case is treated analogously.

Current boundary conditions

Consider first the boundary at $x = 0$, where the ligand source is located. The terms describing the binding and unbinding of the ligand are discretized as above. It remains to take care of the diffusion current $j = -D_0 \partial A/\partial x$ as well as of the source term. In order to derive the correct discretization, let us extend the domain from $x \geq 0$ to the full real axis by reflecting the system at $x = 0$. Suppressing the binding and unbinding terms, the dynamic equation for A then reads

$$\frac{\partial}{\partial t} A = 2\tilde{\nu}\delta(x) - \frac{\partial}{\partial x} j \quad , \tag{28}$$

where $\tilde{\nu} = \nu d/2a^2$. Note, that $j(x) = -j(-x)$. In a small region around $x = 0$ the total number of ligands changes as

$$\frac{d}{dt}\int_{-\varepsilon}^{\varepsilon} A\, dx = \int_{-\varepsilon}^{\varepsilon} \frac{\partial}{\partial t} A\, dx = 2\tilde{\nu} - j(\varepsilon) + j(-\varepsilon) \tag{29}$$

In the limit $\varepsilon \to 0$ this expression must tend to zero, as $\partial A/\partial t$ is continuous in x. This implies

$$\tilde{\nu} = j(0) \quad . \tag{30}$$

Using this result in Eq. (20) we obtain for $n = 0$

$$A_0' = A_0 + \Delta t \left[\frac{\tilde{\nu} - j_1}{\Delta x} - k_{\mathrm{on}} A_0 D_0 + k_{\mathrm{off}} B_0 \right] \quad . \tag{31}$$

In the simulations corresponding to the shibire rescue experiment, that is where we explicitly describe the stripe of Dpp producing cells, the left boundary is chosen to lie in the center of this stripe of cells at $x = -10\mu$m. Assuming the source to be homogeneous, the ligand and receptor concentrations are symmetric with respect to $x = -10\mu$m. Therefore, at this position, the concentration of free ligands has an extremum for all times, i.e., $\partial/\partial x A|_{x=-10\mu\mathrm{m}} = 0$ implying that the current at this position is zero. Therefore, in these simulations we use $j_0 = 0$.

At $x = L$, if there is an impermeable wall for the ligand, then $j(L) = 0$, which implies $j_{N+1} = 0$ in Eq. (20) for $n = N$.

Concentration boundary conditions

The "concentration boundary conditions" chosen in [3] are implemented numerically as follows. At the left boundary $x = 0$,

$$A_0' = A_0 + \Delta t \left[\bar{\nu} - k_{\rm on} A_0 D_0 + k_{\rm off} B_0\right] \quad , \tag{32}$$

where $\bar{\nu}$ is the morphogen production rate in the source. Note, that the units of $\bar{\nu}$ differ from those of $\tilde{\nu}$ and that this equation leads to a violation of the mass balance equation for the ligand. At the right boundary $x = L$, a sink imposes $A(L) = 0$, i.e., $A_N' = A_N = 0$.

AOI SIZE AND BOUNDARY CONDITIONS

In this section we study the influence of the boundary conditions on morphogen gradients in AOIs of different size in the absence of a mutant mosaic in the AOI. The latter condition implies that the ligand and receptor concentrations do not depend on the y-coordinate. Therefore, the profiles of the total ligand concentration $F = A + B + C$ at different times after onset of Dpp production assuming that no Dpp was present initially can be calculated for a one dimensional situation (Fig. S3). Figures S3A,B correspond to an AOI size $L_x = 100\mu$m. The profiles of the total ligand concentration with "current boundary conditions" (Fig. S3B) differ significantly from the ones with "concentration boundary conditions" where the concentration is forced to vanish at $x = L_x$ (Fig. S3A). Using a larger AOI size (200μm), the difference in boundary conditions becomes insignificant (Fig. S3C,D). The AOI chosen in Ref. [3] is $L_x = 100\mu$m, such that the zero concentration boundary conditions at the distal boundary, which implies a sink where the ligand disappears completely, distorts the results. The "current boundary conditions" which we choose have the advantage that the choice of AOI size has a smaller influence on the results.

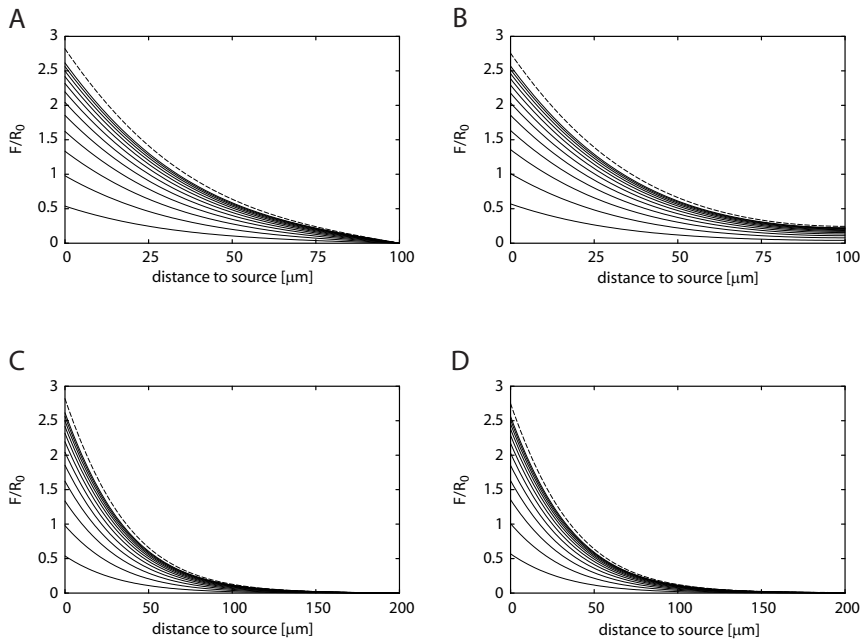

Figure S3. Morphogen gradients in the DBT model for different boundary conditions and AOI sizes. Total ligand concentration F (sum of free extracellular ligand concentration A, surface bound ligand concentration B, and internal bound ligand concentration C) as a function of the distance from the source calculated in the DBT model for different times. Solid curves are separated by intervals of 2h; dashed curve indicates the respective steady state. **A)** Equations (1)-(5) were solved with "concentration boundary conditions" as in [3], i.e., $A = 0$ at $x = L_x$ as well as $\partial A/\partial t = \bar{\nu} - k_{\rm on}A(1-B) + k_{\rm off}B$ at $x = 0$, where $\bar{\nu} = 8 \cdot 10^{-5} s^{-1}$. **B)** Equations (1)-(5) were solved with "current boundary conditions", i.e., $J_x = \nu d/2a^2$ for $x = 0$ and $J_x = 0$ at $x = L_x$. In both cases $L_x = 100\mu$m. Note, that the ligand concentrations differ significantly close to the distal boundary. **C)** Calculation as in (A) ("concentration boundary conditions"), but for $L_x = 200\mu$m. **D)** Calculation as in (B) ("current boundary conditions"), but for $L_x = 200\mu$m. Note that for this size, the ligand profiles do not depend on boundary conditions. Parameters are chosen as in [3], see Table 1 . The value of ν for "current boundary conditions" has been chosen such that $J_x(x = 0)$ equals the ligand current at $x = 0$ in the steady state for "concentration boundary conditions" with $L_x = 200\mu$m. The initial conditions were $A = B = C = 0$, $D = R_0$, and $E = R_0 k_p/k_q$ for all x. Note that the total ligand concentration has been displayed in ordinates normalized to $R_0 = wk_q/k_g k_p$ which is a constant that corresponds to the steady state surface receptor concentration in the absence of ligand.

DYNAMIC EQUATIONS FOR COMPETITION OF GFP-DPP WITH ENDOGENOUS DPP

In the experiments described in Ref. [2] the dynamics of GFP-Dpp occurs on a background of endogenous Dpp, that presumably is in a stationary state. In order to describe the fluorescence intensity of GFP-Dpp, one should therefore in principle distinguish the concentrations A, B and C of nonfluorescent ligand from their GFP tagged counterparts A^*, B^* and C^*, which are observed. This leads to a straightforward generalization of Eqs. (1)-(5):

$$\frac{\partial}{\partial t}A = D_0\nabla^2 A - k_{\rm on}AD + k_{\rm off}B \tag{33}$$

$$\frac{\partial}{\partial t}A^* = D_0\nabla^2 A^* - k_{\rm on}A^*D + k_{\rm off}B^* \tag{34}$$

$$\frac{\partial}{\partial t}B = k_{\rm on}AD - (k_{\rm off}+k_{\rm in})B + k_{\rm out}C \tag{35}$$

$$\frac{\partial}{\partial t}B^* = k_{\rm on}A^*D - (k_{\rm off}+k_{\rm in})B^* + k_{\rm out}C^* \tag{36}$$

$$\frac{\partial}{\partial t}C = k_{\rm in}B - (k_{\rm out}+k_{\rm deg})C \tag{37}$$

$$\frac{\partial}{\partial t}C^* = k_{\rm in}B^* - (k_{\rm out}+k_{\rm deg})C^* \tag{38}$$

$$\frac{\partial}{\partial t}D = k_{\rm off}(B+B^*) + k_{\rm q}E - k_{\rm on}(A+A^*)D - k_{\rm p}D \tag{39}$$

$$\frac{\partial}{\partial t}E = w + k_{\rm p}D - (k_{\rm q}+k_{\rm g})E \tag{40}$$

Furthermore, we introduce the production rate ν^* of GFP-Dpp. The levels of expression of GFP-Dpp are about five times higher than those of the endogenous Dpp as assessed by quantitative RT-PCR and Western blots to monitor the RNA and protein level (not shown).

Figure S4 shows that the profiles of GFP-Dpp in the presence of endogenous Dpp obtained from Eqs. (33)-(40) are very similar to the profiles obtained with the DBT model, Eqs. (1)-(5). Here, the secretion rate ν^* of GFP-Dpp is seven times that of the secretion rate ν of endogenous Dpp. Note, that for the parameter values given in Table 1 , this result is independent of the ratio of the production rates ν and ν^* of endogenous Dpp and GFP-Dpp, resp., as long as the total Dpp production rate, $\nu+\nu^*$, is constant. This is a consequence of the fraction of ligand bound surface receptors being low. For simplicity, all results shown in the paper are therefore obtained by assuming that the presence of endogenous Dpp can be neglected.

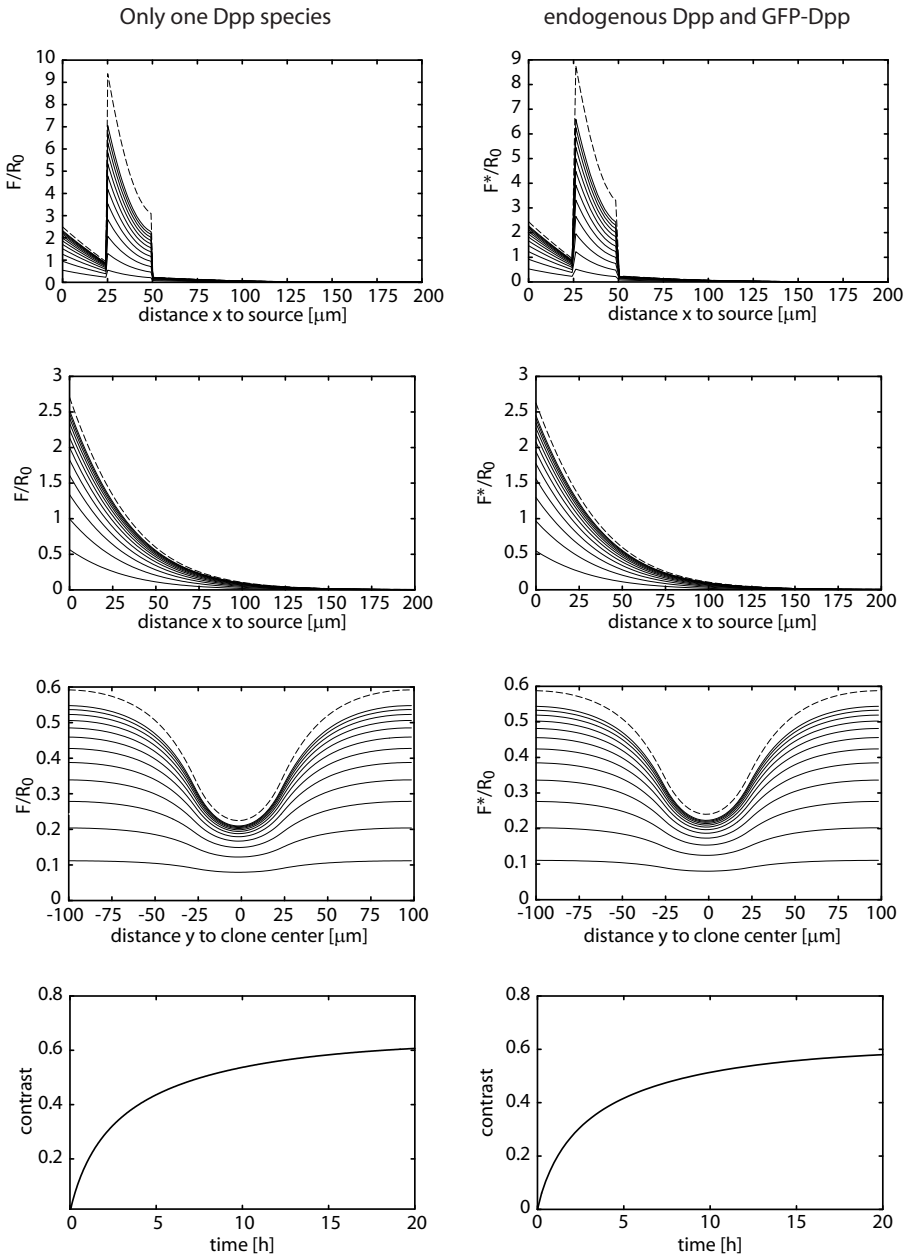

Figure S4. Competition of GFP-Dpp with endogenous Dpp. Total GFP-Dpp profiles obtained from a two-dimensional calculation of the DBT model in which endogenous Dpp and GFP-Dpp were treated seperately according to Eqs. (33)-(40) compared to those obtained from the calculation shown in Fig. 3. The same geometry and parameters as depicted in Fig. 3 were applied. The production rate of GFP-Dpp was chosen seven times larger than that of endogenous Dpp.

The situation is different in the DBTS model. In particular, if we describe the experimental situation of a patch of dynamin deficient cells in the receiving tissue using the DBTS model with the parameters values given in Table 1 , the maximal concentration of surface receptors $R_{\max}$ has to be increased in order to obtain shadows of the same contrast as in the case without endogenous Dpp.

SPECIFICITY OF THE TKV ANTIBODIES

In Fig. S5 we provide the data showing that the anti-Tkv antibodies are specific.

[1] B. Alberts *et al.*, *Molecular Biology of the Cell* 4th ed. (Garland, New York, 2002)

[2] Entchev, E.V., Schwabedissen, A., and Gonzáles-Gaitán, M. (2000), Cell *103*, 981-991.

[3] Lander, A.D., Nie, Q., and Wan, F.Y.M. (2002), Dev. Cell *2*, 785-796.

Figure S5. Detecting total and cell surface Thickveins. **A)** Wild-type third instar wing disc stained with anti-Tkv antibody. Thickveins predominantly outlines the cells and forms a gradient inversed with respect to the Dpp gradient. The Tkv counter-gradient has a shallow slope and might not be very apparent in some cases, depending on the imaging conditions. **B,C)** Tkv immunostainings of third instar wing discs expressing *UAS-Tkv* under the *ptc-gal4* driver using anti-Tkv (B) or anti-Tkv blocked by its corresponding peptide antigen (C). Note that the anti-Tkv antibody detects overexpression levels of Tkv induced by the Gal4 system whereas it is abolished when performing a protocol where prior to immunostaining the antibody was incubated with its corresponding target polypeptide. Other polypeptides did not have any effect. Fold in the wing pouch is caused by Tkv overexpression. **D)** Double labeling showing tkv^8 clones marked by the absence of PMyc (red) and Tkv immunostaining (green). Genotype: *HS-Flp/+; M(2)z PMyc FRT40A/*tkv^8 *FRT40A*. The anti-Tkv antibody does not stain cells lacking Tkv in mutant mosaics present in the notum of a third instar wing disc. (*Caption continued on next page.*) **E)** Wild-type third instar wing disc showing immunostaining of cell surface exposed Tkv using the Tkv luminal antibody and the extracellular immunostaining protocol. The level of surface Thickveins is decreased within a narrow stripe of cells located anterior to the anterior-posterior compartment boundary.

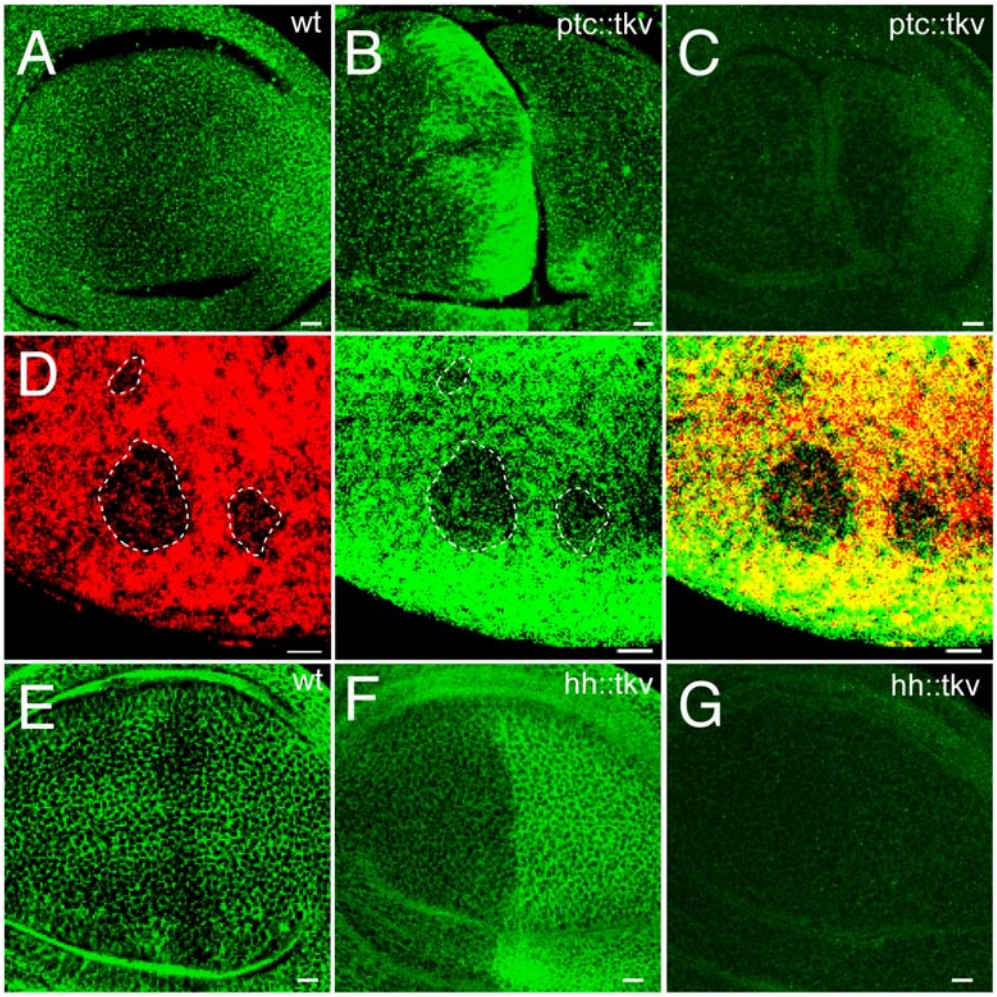

Figure S5 continued. **F,G)** Immunostaining of cell surface exposed Tkv of third instar wing discs expressing *UAS-Tkv* under the *hh-gal4* driver; using luminal anti-Tkv (F) or luminal anti-Tkv antibody blocked by its corresponding peptide antigen (G). Note that the luminal anti-Tkv antibody detects overexpression levels of cell surface exposed Tkv induced by the Gal4 system, whereas it is abolished when incubated with its corresponding target polypeptide. Bars correspond to 10μm.